RESEARCH PAPER

A three-dimensional multi-surface plasticity soil model for seismically-induced liquefaction and earthquake loading applications

Zhijian Qiu[1] · Athul Prabhakaran[2] · Ahmed Elgamal[2]

Abstract

This paper presents a three-dimensional (3D) multi-surface plasticity model to computationally simulate the behavior of coarse-grained granular soil during seismically-induced liquefaction. The model extends an existing multi-surface plasticity formulation and includes the Lade–Duncan failure criterion as the yield function to more closely capture salient characteristics of laboratory test data. Subsequently, flow rules are updated for modeling the essential shear response mechanisms associated with dilatancy, cyclic mobility, and post-liquefaction shear strain accumulation. The constitutive model is implemented into the OpenSees computational framework, and Finite Element (FE) calibrations are undertaken to match a set of laboratory test data, including drained monotonic/undrained stress-controlled cyclic triaxial tests, and a centrifuge test on a liquefiable sloping ground. It is demonstrated that the soil constitutive model and the employed computational framework can reasonably predict the seismic response of the liquefiable sloping ground under earthquake loading. On this basis, full 3D FE simulations of a typical bridge abutment seated on liquefiable sloping ground are conducted to further highlight underlying earthquake-induced liquefaction effects on the ground-structure system deformations. Overall, the developed constitutive model provides a useful tool for evaluating earthquake-induced soil liquefaction hazards and associated 3D ground seismic response scenarios.

Keywords Cyclic mobility · Earthquake · Finite element · Liquefaction · Multi-surface · Three-dimensional

1 Introduction

Soil liquefaction is a major cause of earthquake-induced damage to the built environment. Previous earthquakes have indicated that liquefaction may trigger substantial permanent downslope deformation in sloping ground, thus causing extensive damage to the bridge abutments, pile foundations, and buildings [2, 21, 43, 46, 49, 53]. Such

detrimental effects of soil liquefaction occurred in recent earthquakes, such as the 2010 El Mayor-Cucapah [44], the 2010 Maule [30], and the 2011 Christchurch earthquakes [10].

To numerically simulate soil liquefaction, a number of constitutive models have been developed [1, 3, 9, 11, 15–17, 26, 41, 48, 50–52, 56]. For instance, Boulanger and Ziotopoulou [4] present a plane strain soil plasticity model calibrated with empirical guidelines on liquefaction triggering for geotechnical earthquake engineering applications, following the framework of bounding surface plasticity [11]. Iai et al. [22] proposed a two-dimensional (2D) strain space multiple mechanism model by relating micromechanical structures to the macroscopic deformation of granular materials. Wang et al. [47] developed a unified plasticity sand model based on critical state soil mechanics for modeling the cyclic behavior and large post-liquefaction shear deformation.

To further understand saturated coarse-grained soil behavior associated with liquefaction, LEAP (Liquefaction

✉ Zhijian Qiu
ZhijianQiu@xmu.edu.cn

Athul Prabhakaran
aparayan@eng.ucsd.edu

Ahmed Elgamal
elgamal@ucsd.edu

1 Fujian Key Laboratory of Digital Simulations for Coastal Civil Engineering, Department of Civil Engineering, Xiamen University, Xiamen 361005, Fujian, China

2 Department of Structural Engineering, UC San Diego, La Jolla, CA 92093, USA

Experiments and Analysis Projects) conducted a series of laboratory element tests and centrifuge experiments on gently sloping ground at different facilities [28, 32]. Motivated by the high-quality experimental data of LEAP, many efforts were undertaken to validate the capabilities of existing soil constitutive models [7, 13, 18, 37, 54, 58]. Among these, the OpenSees PDMY03 material [15, 16, 26, 50, 52] demonstrated potential to predict the seismic response of liquefiable sloping ground. However, the PDMY03 material employs the Drucker–Prager J_2 yield criterion as the yield function, leading to unrealistic strength estimates, as pointed out earlier [29]. As shown in Fig. 1a, the circular failure surface of the Drucker–Prager criterion in the deviatoric stress plane can only capture one particular triaxial loading path (compression or extension) of the well-known Lade–Duncan function which is verified by a large number of laboratory sample test data on granular soils, thus poorly approximating other loading paths (i.e., non-overlapping zone in Fig. 1a). Ultimately, it is challenging to use this PDMY03 material to realistically reproduce the asymmetric axial strain accumulation pattern typically exhibited in undrained stress-controlled cyclic triaxial tests (e.g., Fig. 1b) and the subsequent liquefaction triggering of sand with various relative densities under different shear stress levels [28, 32].

As such, the OpenSees PDMY03 material is extended to include the Lade–Duncan failure criterion [29] as the yield function, allowing for considerable accuracy in 3D shear response conditions (source codes are available at https://doi.org/10.5281/zenodo.7539808.). Subsequently, flow rules are updated to more closely capture the salient characteristics of laboratory test data, including cyclic mobility, dilatancy, and post-liquefaction shear strain accumulation. The updated soil constitutive model is verified and validated by a set of laboratory test data and a

centrifuge test on a liquefiable sloping ground [28, 32]. Finally, a system-level simulation of a typical pile-supported bridge abutment in liquefiable sloping ground is considered to investigate the earthquake-induced liquefaction effects on ground-structure seismic response.

The following sections of this paper outline: (1) the main formulations of the constitutive model, (2) model calibration processes, (3) simulation of a centrifuge test for liquefiable sloping ground, (4) earthquake loading applications, and (5) insights derived from this study. Finally, conclusions are summarized and discussed.

2 Model description

2.1 Yield function

The OpenSees multi-surface plasticity material (i.e., PDMY03) [26] is extended to include the Lade–Duncan failure criterion [29] as the yield function, and a typical surface $\{f_m\}$ (Fig. 2) is defined as:

$$f_m = \overline{J}_3 - \frac{1}{3}(\eta_m I_1)\overline{J}_2 + a_1(\eta_m I_1)^3 = 0 \tag{1}$$

where η_m denotes normalized yield surface size ($0 < \eta_m < 1$), m denotes the yield surface number beginning from 1 to NYS (the total number of yield surfaces), I_1 represents the first stress invariant, and parameter $a_1 = \left[\frac{2sin\phi}{3(3-sin\phi)}\right]^2 - 2\left[\frac{2sin\phi}{3(3-sin\phi)}\right]^3$ is related to soil shear strength in terms of friction angle ϕ based on triaxial compression [8]. In Eq. (1), $\overline{J}_2 = \frac{1}{2}\overline{s} : \overline{s}$ and $\overline{J}_3 = \frac{1}{2}(\overline{s} \cdot \overline{s}) : \overline{s}$, where, $\overline{s} = s - p'a$ and $s = \sigma - p'\delta$, σ denotes stress tensor, δ represents the second-order identity tensor, $p' = \frac{1}{3}I_1$ is effective
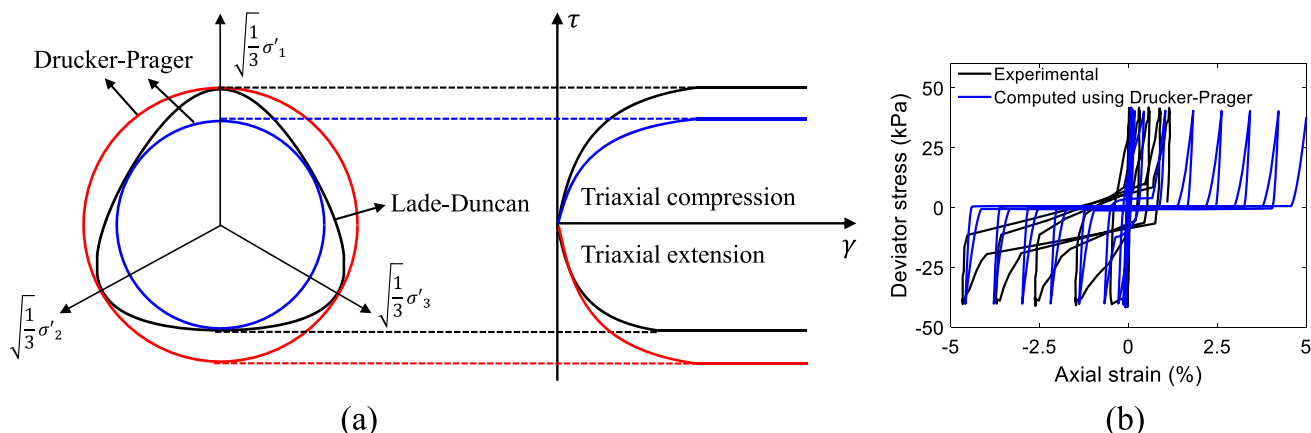

Fig. 1 Comparison between Lade–Duncan and Drucker–Prager failure criterion: **a** Schematic of drained monotonic triaxial compression and extension test; **b** Experimental and computed undrained cyclic stress-controlled triaxial test using a Drucker–Prager multi-surface soil model
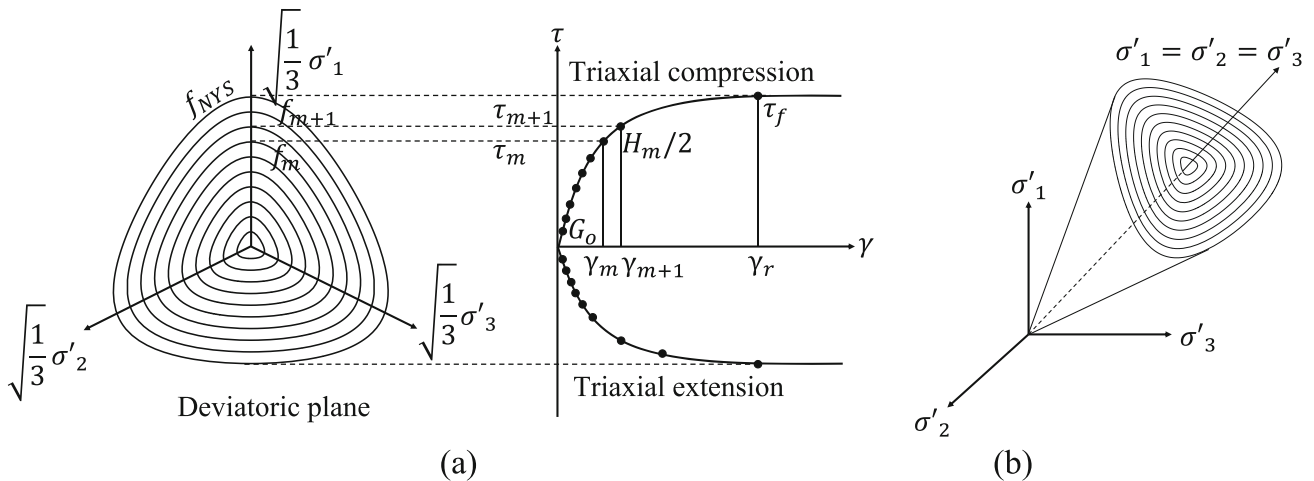
Fig. 2 The multi-surface plasticity model with Lade–Duncan failure criterion: **a** Octahedral shear stress and strain; **b** Yield surfaces in principal stress space

confinement, $\boldsymbol{a}$ is back stress (i.e., the center of the yield surface), and the operators "·" and ":" denote the single and double contraction of two tensors, respectively.

2.2 Piecewise linear approximation of yield surfaces

In this model, the shear-strain backbone curve (Fig. 2a) is represented by the following hyperbolic relationship:

$$\tau = \frac{G\gamma}{1 + \gamma/\gamma_r} \tag{2}$$

where the low-strain shear modulus is defined as $G = G_0\left(p'/p_r'\right)^n$, p_r' denotes the reference effective confinement, γ_r is the reference shear strain computed as $\gamma_r = \frac{\gamma_{max}\tau_{max}}{G\gamma_{max}-\tau_{max}}$, τ_{max} is the shear strength that corresponds to the shear strain γ_{max} (Fig. 2a), G_0 is the shear modulus at p_r', and d is the dependency of shear modulus on p_r' (taken as $d = 0.5$ in this study). Within the multi-surface plasticity framework, a set of *NYS* yield surfaces form the hardening zone with different sizes. As such, the piecewise linear approximation of the hyperbolic backbone curve defined by *NYS* stress–strain pairs is given as:

$$\tau_m = \tau_{max}\frac{m}{NYS}, \gamma_m = \frac{\tau_m\gamma_r}{G\gamma_r - \tau_m} \tag{3}$$

Each line segment (Fig. 2a) represents the domain of a yield surface $\{f_m\}$ characterized by a constant size $K^{(m)} = 3\tau_m/\sqrt{2}$, and an elasto-plastic shear modulus $H^{(m)} = 2\left(\frac{\tau_{m+1}-\tau_m}{\gamma_{m+1}-\gamma_m}\right)/p_r'$. In general, conventional (user defined) shear modulus reduction curves can be also

employed for the specification of yield surface characteristics including sizes and elasto-plastic moduli.

2.3 Flow rule

A non-associative flow rule [15, 16, 26, 50, 52] is employed to handle the interaction between shear and volume change, including contraction and dilation. In this model, the outer normal to the plastic potential surface and the yield surface ($\boldsymbol{P}$ and $\boldsymbol{Q}$) can be decomposed into volumetric and deviatoric components as $\boldsymbol{P} = \boldsymbol{P}' + P''\boldsymbol{\delta}$ and $\boldsymbol{Q} = \boldsymbol{Q}' + Q''\boldsymbol{\delta}$. Similar to the PDMY03 model formulations, the volumetric component of the flow rule is non-associative (i.e., $P'' \neq Q''$), and associativity is only restricted to the deviatoric component (i.e., $\boldsymbol{P}' = \boldsymbol{Q}'$). According to the yield function (Eq. 1), the outer normal to a typical surface $\{f_m\}$ can be obtained by:

$$\boldsymbol{Q} = \frac{\partial f_m}{\partial \boldsymbol{\sigma}} / \sqrt{\frac{\partial f_m}{\partial \boldsymbol{\sigma}} : \frac{\partial f_m}{\partial \boldsymbol{\sigma}}} \tag{4}$$

$$\begin{aligned}
\frac{\partial f_m}{\partial \boldsymbol{\sigma}} = &\ \overline{\mathbf{S}} \cdot \overline{\mathbf{S}} - \left(\frac{1}{3}\eta_m I_1\right)\overline{\mathbf{S}} \\
&- \frac{1}{3}\Big[(2 + \eta_m)\overline{J}_2 + (\overline{\mathbf{S}} \cdot \overline{\mathbf{S}}) : \boldsymbol{a} \\
&- \frac{1}{3}\eta_m I_1\overline{\mathbf{S}} : \boldsymbol{a} + 3a_1\eta_m^3 I_1^2\Big]\boldsymbol{\delta}
\end{aligned} \tag{5}$$

Based on the stress state at the last time step (i), the deviatoric stress $\boldsymbol{s}$ and effective confinement p' at the current time step ($i + 1$) are updated as follows:

$$p'_{i+1} = p'_i + 3BP''L \qquad (6)$$

$$s_{i+1} = s_i - 2GQ'L \qquad (7)$$

where B represents the bulk modulus, L is the plastic loading function determined by $Q : \dot{\sigma}/H'$ [15, 16, 26, 35, 50, 52], $\dot{\sigma}$ denotes the rate of stress tensor, H' is plastic modulus and computed as $2G_0 H^{(m)}/(2G_0 - H^{(m)})$.

2.3.1 Phase transformation surface

Following the pioneering efforts by Ishihara [24], a straight phase transformation (PT) line in stress space is employed as the boundary to separate two distinct zones where soil behavior is dilative or contractive under shear loading (Fig. 3). In current model, the PT surface is simply defined by the constant PT angle (ϕ_{PT}) and does not evolve with the stress path. According to the relative location of stress state with respect to the PT surface, distinct contractive or dilative behavior is defined by comparing the stress ratio η to that along the PT surface (i.e., η_{PT}). For stress state inside (or outside) the PT surface, i.e., $\eta < \eta_{PT}$ (or $\eta > \eta_{PT}$), a tendency of contraction (or dilation) is defined, resulting in decreased (or increased) effective confinement p' [15, 16, 26, 35, 50, 52]. As such, appropriate expressions for volumetric component for P'' in Eq. (6) should be specified to account for the change of effective confinement p' under undrained conditions, as discussed below.

2.3.2 Contractive phase

Shear-induced contraction appears inside the PT surface (i.e., $\eta < \eta_{PT}$), or outside (i.e., $\eta > \eta_{PT}$) when unloading occurs (such as stages 0–1, 2–3, 3–4, 6–7 in Fig. 3), where $\eta = \sqrt{\frac{3}{2} s : s}/p'$ represents the deviatoric stress ratio, and η_{PT} denotes the deviatoric stress ratio at the PT surface. To closely capture the salient characteristics of laboratory test data, the volumetric component P'' (Eq. 6) is updated in accordance with experimental observations as:

$$P'' = (c_1 + c_2\gamma_c)(p'/p_a)^{c_3}(c_4\eta_{OCT})^{c_5} \qquad (8)$$

during all previous dilation phases (i.e., summing all $\Delta\gamma_c$ in Fig. 3b), p_a represents atmospheric pressure, and η_{OCT} is the octahedral shear stress ratio. The parameter c_3 in Eq. (8) defines the dependence of pore pressure buildup on initial confinement (i.e., K_σ effect).

2.3.3 Dilative phase

Dilation (such as stages 1–2, 5–6, 8–9 in Fig. 3) is defined as shear plastic loading outside the PT surface (i.e., $\eta > \eta_{PT}$), and is given as:

$$P'' = (d_1 + \gamma_d^{d_2})(p'/p_a)^{-d_3}(\eta_{OCT})^{d_4} \qquad (9)$$

where d_1, d_2, d_3, and d_4 are non-negative calibration constants, and γ_d denotes the octahedral shear strain accumulated from the beginning of a particular dilation cycle (e.g., stage 1–2, 5–6 or 8–9 in Fig. 3). Consequently, a dilation tendency increases as the shear strain accumulates in this cycle, as experimentally observed by Kabilamany and Ishihara [25]. It should be noted that significant unloading (e.g., stages 2–3 or 6–8 in Fig. 3) will reset γ_d to zero. Similarly, parameter d_3 in Eq. (9) reflects the influence of initial confinement on pore pressure buildup (i.e., K_σ effect).

2.3.4 Neutral phase

When the shear stress approaches the PT surface (i.e., $\eta = \eta_{PT}$) from contraction, permanent shear strain [15, 16, 26, 50, 52] prior to dilation will accumulate with minimal changes in shear stress and confinement (implying $P'' \approx 0$, such as stages 4–5 and 7–8 in Fig. 3), as observed in laboratory test data from Ishihara [24]. Nevertheless, it is difficult to reasonably capture the minimal change in this stress state for reproducing the associated accumulation of post-liquefaction shear strain. In this study, $P'' = 0$ (Eq. 6) is assumed for simplicity and maintained until the boundary of yield domain defined in deviatoric strain space is reached. Following the earlier studies by Yang et al. [52], this strain space mechanism is a phenomenological approach to reproduce the soil response in accordance with

$$\eta_{OCT} = \frac{\frac{1}{3}\sqrt{\left[(\sigma_{11} - \sigma_{22})^2 + (\sigma_{22} - \sigma_{33})^2 + (\sigma_{11} - \sigma_{33})^2\right]/2 + 6\tau_{12}^2 + 6\tau_{23}^2 + 6\tau_{13}^2}}{p'}$$

where c_1, c_2, c_3, c_4, and c_5 are non-negative calibration constants, γ_c denotes octahedral shear strain accumulated

experimental observations, and the yield domain can be enlarged or translated depending on the load history.
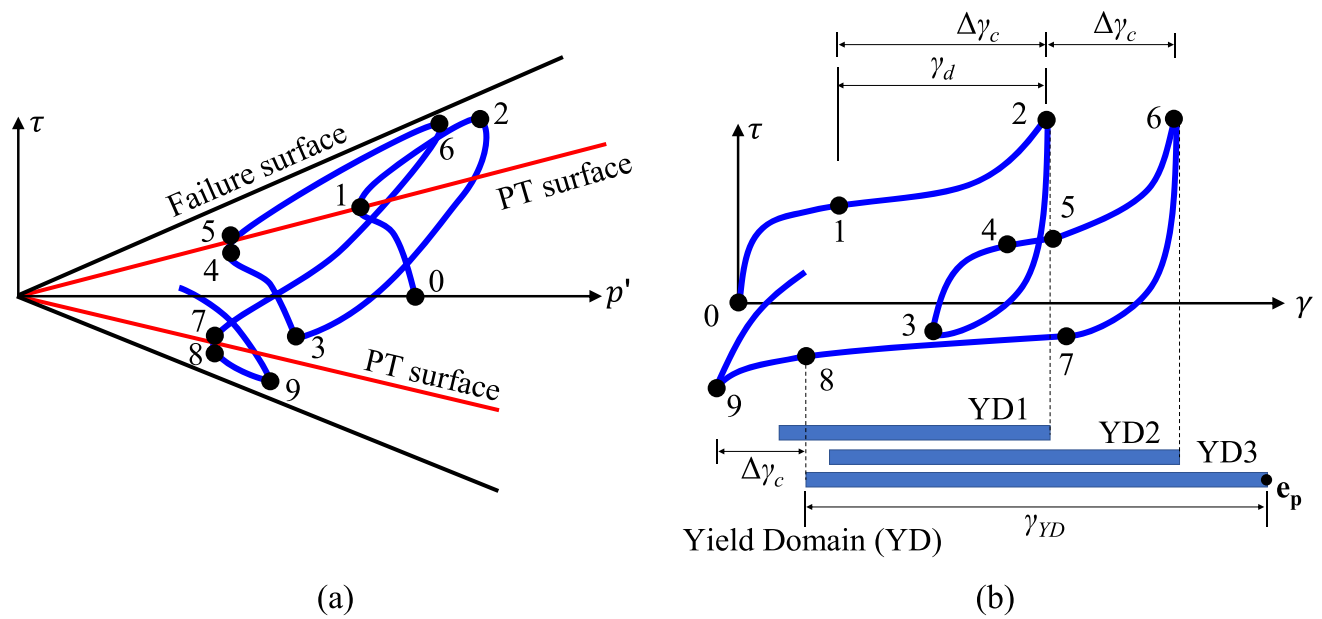
Fig. 3 Illustration of constitutive model response: **a** Shear stress-confinement; **b** Shear stress-shear strain with yield domain evolution

The yield domain in the previous formulation [52] is activated only for confinement lower than a user-specified value (e.g., 10 kPa). In addition, the increment of the yield domain size during each loading phase is restricted to a user-specified maximum value (e.g., 2%). Nonetheless, the liquefaction-induced shear deformation under cyclic loading can be accumulated continuously in a cyclic-by-cycle pattern [24]. As such, the yield domain (i.e., γ_{YD} as shown in Fig. 3b) size can be defined as a function of accumulated shear strain and effective confinement histories during cyclic loading, without the need for prescribing a particular confinement to activate the strain space mechanism. Specifically, the yield domain size is defined in terms of the accumulated octahedral shear strain γ_s as a function of dilation history and octahedral shear strain γ_{rv} as a function of load reversal history:

$$\gamma_{YD} = \gamma_s + \gamma_{rv}$$
$$\gamma_s = y_1 \left\langle \frac{p'_{max} - p'_n}{p'_{max}} \right\rangle^{0.25} (\eta_{OCT})^{y_2} \int_0^t \Delta\gamma_c \qquad (10)$$
$$\gamma_{rv} = y_3 \left\langle \frac{p'_{max} - p'_n}{p'_{max}} \right\rangle^{0.25} oct(e - e_p)$$

where, y_1, y_2 and y_3 are non-negative calibration constants, p'_{max} is maximum mean effective confinement experienced during cyclic loading, p'_n is mean effective confinement at the beginning of the neutral phase, $\int_0^t \Delta\gamma_c$ represents the octahedral shear strain accumulated during previous

dilative phases (such as stages 1–2, 5–6 and 8–9 in Fig. 3), $\langle\rangle$ denotes MacCauley's brackets (i.e., $\langle a \rangle = max(a, 0)$), $oct(e - e_p)$ defines the octahedral shear strain of the $e - e_p$ tensor, where e is the current deviatoric shear strain, and e_p is pivot strain obtained from the previous dilation on load reversal point (Fig. 3). As such, Eq. (10) allows for continued enlargement of the domain size in proportion to (1) shear strain accumulated during previous dilative phases, and (2) reduction in mean effective confinement.

For illustration, Fig. 4a shows the effect of parameter y_1 on the accumulation of axial strain for an undrained stress-controlled cyclic triaxial loading simulation. As seen in this figure, a larger y_1 will result in a higher level of cycle-by-cycle axial strain accumulation (Fig. 4a). The effect of y_2 on the asymmetric accumulation of normalized axial strain is investigated in Fig. 4b. It can be seen that larger y_2 causes a comparatively lower level of deformation in triaxial compression (Fig. 4b). The y_3 parameter is mainly used to define the biased accumulation of permanent shear strain γ_{rv} as a function of load reversal history and allows for translation of the yield domain according to the pivot strain e_p [52] during cyclic loading.

2.4 Hardening rule

A purely deviatoric kinematic hardening rule is adopted to reproduce the hysteretic response under cyclic loading conditions. For translation of active yield surface $\{f_m\}$ after
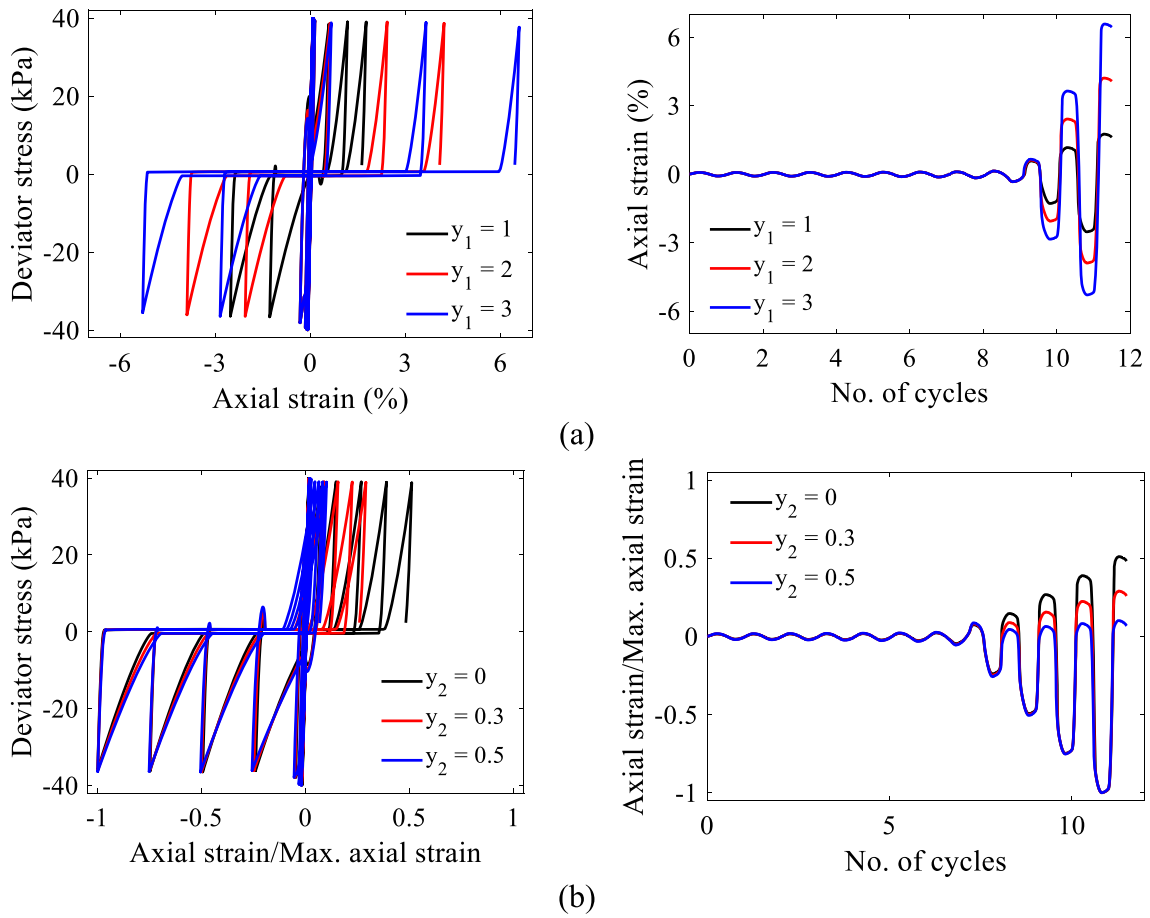
Fig. 4 Post-liquefaction strain accumulation: **a** Effect of y_1; **b** Effect of y_2
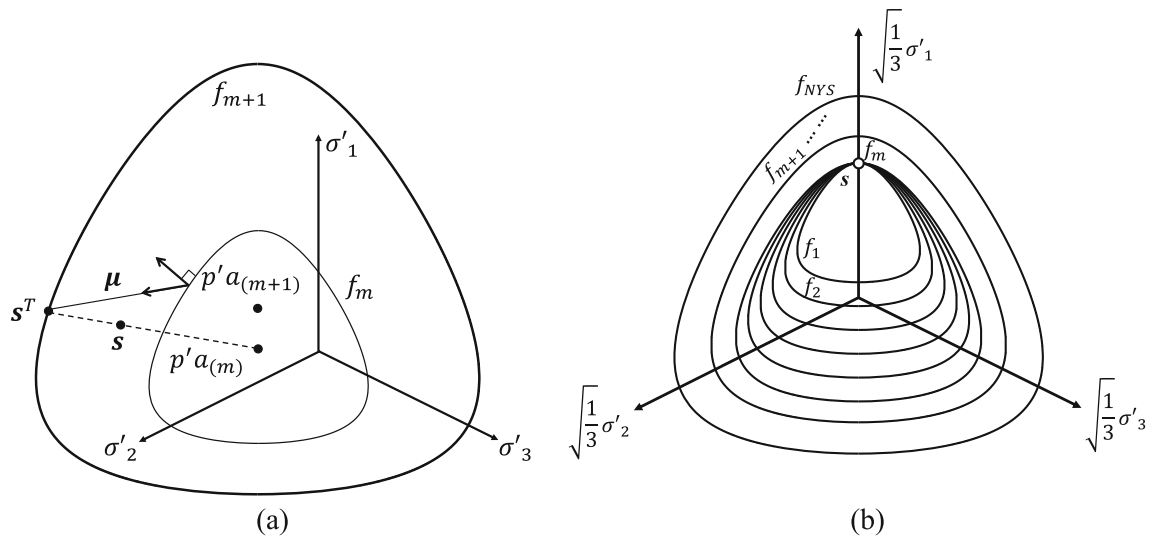

Fig. 5 Yield surface translation in deviatoric plane: **a** Updated of active surface; **b** Update of inner surface
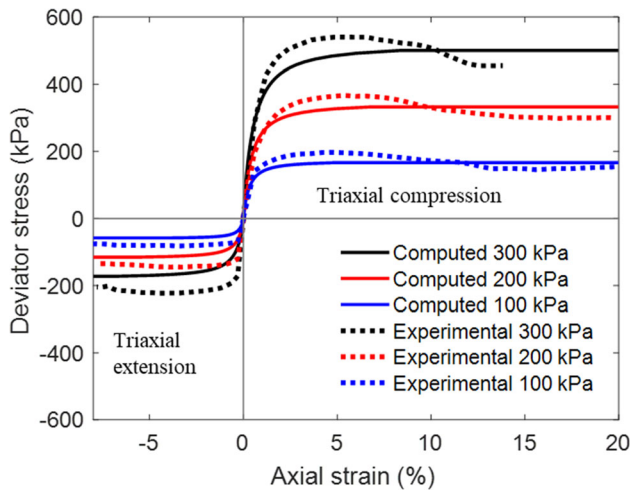
Fig. 6 Experimental and computed results of drained monotonic triaxial tests for Ottawa sand with relative density $D_r = 65\%$

the updated shear stress s is determined (Fig. 5a), no overlapping is allowed between yield surfaces $\{f_m\}$ and $\{f_{m+1}\}$ according to the logic described in Elgamal et al. [16]. On this basis, the direction of translation as displayed in Fig. 5a is defined as:

$$\boldsymbol{\mu} = \left[\boldsymbol{s}^T - p'\boldsymbol{a}^{(m)}\right] - \frac{\eta_m}{\eta_{m+1}}\left[\boldsymbol{s}^T - p'\boldsymbol{a}^{(m+1)}\right] \quad (11)$$

where $\boldsymbol{s}^T$ denotes the intersection of the outer yield surface $\{f_{m+1}\}$ and the vector connecting the active surface center $p'\boldsymbol{a}^{(m)}$ and the updated stress state $\boldsymbol{s}$. The stress $\boldsymbol{s}^T$ is assumed to be $x\left[\boldsymbol{s} - p'\boldsymbol{a}^{(m)}\right]$ and the unknown scalar x (≥ 1) can be solved from the condition that $\boldsymbol{s}^T$ satisfies the yield function of the outer yield surface (i.e., $\{f_{m+1} = 0\}$ in Eq. 1). Thereafter, the magnitude of translation $\lambda\boldsymbol{\mu}$ or the new center $\boldsymbol{a}_{New}^{(m)} = \boldsymbol{a}^{(m)} + \lambda\boldsymbol{\mu}$, where λ is a positive scalar, can be obtained by enforcing the consistency condition that the updated stress state $\boldsymbol{s}$ satisfies the yield function of the yield surface $\{f_m = 0\}$. Upon load reversal, the locations of all inner yield surfaces (i.e., $\{f_1\}$, $\{f_2\}$,…, $\{f_{m-1}\}$) are updated, such that $\{f_1\}$ to $\{f_m\}$ are tangent to each other at the current shear stress point $\boldsymbol{s}$ (Fig. 5b). Finally, translation of all inner yield surfaces ($\{f_1\}$, $\{f_2\}$,…, $\{f_{m-1}\}$) is controlled by:

$$\frac{\boldsymbol{s} - \boldsymbol{a}^{(m)}}{K^{(m)}} = \frac{\boldsymbol{s} - \boldsymbol{a}^{(m-1)}}{K^{(m-1)}} = \cdots = \frac{\boldsymbol{s} - \boldsymbol{a}^{(1)}}{K^{(1)}} \quad (12)$$

Table 1 Sand model parameters

Model parameters (D_r)	65%	75%	85%	95%[a]
Reference mean effective pressure, p'_r (kPa)	101	101	101	101
Mass density, ρ (t/m³)	2.04	2.08	2.12	2.2
Maximum shear strain at p'_r, γ_{max}	0.1	0.1	0.1	0.1
Low-strain shear modulus at p'_r, Go (MPa)	20	25	30	80
Stiffness dependence coefficient d, $G = Go\,(p'/p'_r)^d$	0.5	0.5	0.5	0.5
Poisson's ratio v (for dynamics)	0.4	0.4	0.4	0.4
Shear strength at zero confinement, c (kPa)	0.3	0.3	0.3	0.3
Friction angle, ϕ	40°	42°	44°	46°
Phase transformation angle, ϕ_{PT}	26°	26°	26°	26°
Contraction coefficients, c_1	0.15	0.08	0.02	0.01
Contraction coefficients, c_2	100	50	200	1
Contraction coefficients, c_3	0.1	0.1	0.1	0
Contraction coefficients, c_4	2.0	1.5	1.5	0.0
Contraction coefficients, c_5	1.1	1.1	1.1	1.0
Dilation coefficient, d_1	0.15	0.3	0.5	0.8
Dilation coefficient, d_2	3	3	3	3
Dilation coefficient, d_3	0.3	0.3	0.3	0.3
Dilation coefficient, d_4	2.0	1.5	1.5	0
Damage parameter, y_1	1	1	1	1
Damage parameter, y_2	0.3	0.5	0.5	0
Damage parameter, y_3	0	0	0	0

[a]Assumed properties of very dense sand layer as displayed in Fig. 14

3 Model calibration

3.1 Drained monotonic triaxial tests

This section attempts to determine the friction angle ϕ and low-strain shear modulus G_0 defined in the hyperbolic backbone curve to provide a basis for further calibration of Ottawa sand related to liquefaction (discussed below). As such, six drained monotonic triaxial compression/extension tests of Ottawa sand with relative density $D_r = 65\%$ at confining pressures p'_0 of 100, 200, and 300 kPa [45] are simulated by using the developed constitutive model. The shear modulus G_0 and friction angle ϕ are evaluated by matching the initial slope and the peak strength of the stress–strain curves in these drained monotonic triaxial tests (Fig. 6). In addition, the reference mean effective pressure p'_r, Poisson's ratio v and maximum shear strain γ_{max} (Fig. 2) are assumed to be one atmosphere (i.e., 101 kPa), 0.4 and 0.1 respectively. The mass density ρ is obtained from the initial void ratio and specific gravity provided by Vasko [45]. Following the previous studies by
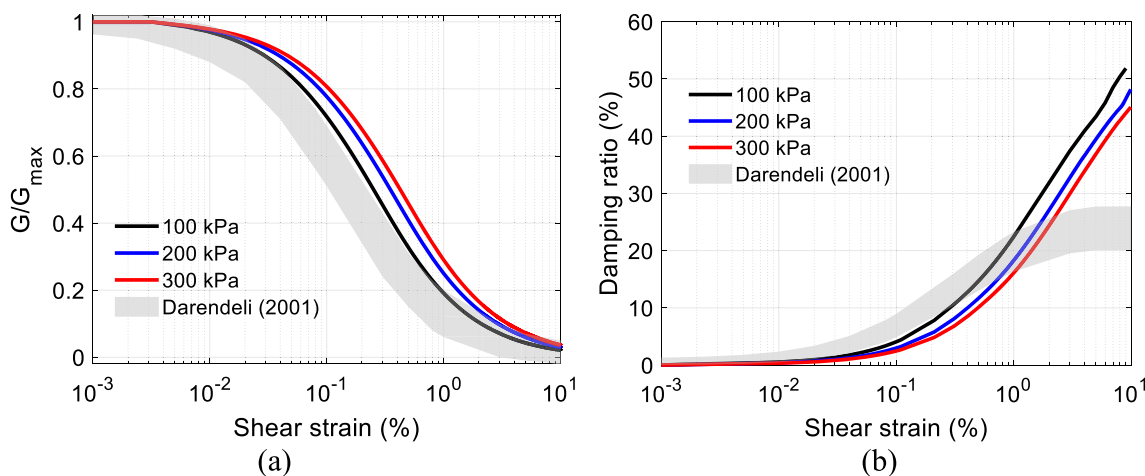
Fig. 7 Behavior of Ottawa sand with relative density $D_r = 65\%$ under an effective confinement of 100, 200 and 300 kPa: **a** Shear modulus reduction curve; **b** Damping ratio curves (Darendeli [12] with $\gamma_r = 0.15$ employed)
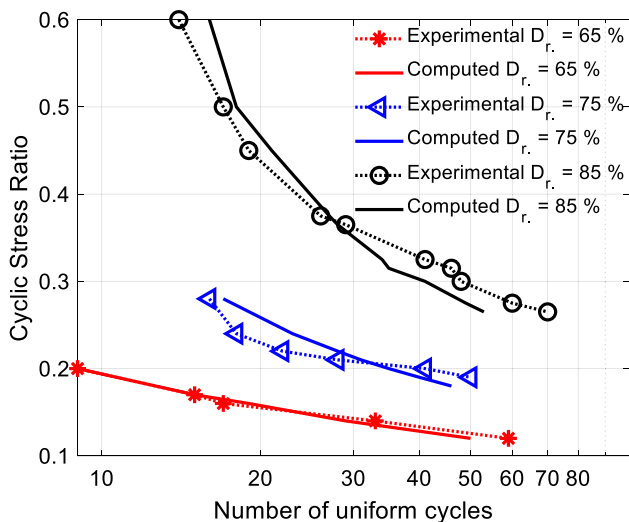

Fig. 8 Experimental and computed liquefaction strength curves of Ottawa sand with relative densities $D_r = 65$, 75, and 85%

Yang et al. [52], the shear strength c at zero confinement is taken as 0.3 kPa for simplicity.

With the calibrated values in Table 1, the computed backbone curves of Ottawa sand under drained compression/extension conditions show reasonable overall agreement with the experimental counterpart at various confining pressures p'_0 (Fig. 6). For illustration, Fig. 7 displays the shear modulus reduction and damping ratio curves produced by the calibrated model. Generally, these results are greater than those recommended empirically (e.g., Darendeli [12]), as discussed in Ramirez et al. [40].

3.2 Undrained stress-controlled cyclic triaxial tests

In this section, the constitutive model parameters associated with shear-induced contraction (c_1–c_5), dilation (d_1–d_4) and post-liquefaction strain accumulations (y_1–y_3) are determined based on 21 undrained stress-controlled cyclic triaxial tests [19]. Specifically, parameters c_1, c_2, c_4, and c_5 are iteratively calibrated by matching the liquefaction strength curves of the Ottawa sand with relative densities $D_r = 65$, 75, and 85%. In addition, parameters d_1, d_4, and y_3 are adjusted to improve the comparison of the computed results to the stress path and post-liquefaction shear strain accumulation from the undrained cyclic triaxial tests. It is noted that (1) the parameters c_3, d_2, d_3, y_1, and y_2 are essentially constant for all relative densities, similar to the PDMY03 material [26], and (2) With an increase in D_r, c_1 reduces whereas d_1 increases, due to the reduced contractive tendency and increased dilative tendency of denser sand. Finally, the developed constitutive model is implemented into the computational platform OpenSees [33], and the source codes (C++ based) are available at https://doi.org/10.5281/zenodo.7539808.

With the modeling parameters discussed in Table 1, Fig. 8 depicts the liquefaction strength curves of the Ottawa sand (i.e., number of cycles to reach 2.5% single amplitude of axial strain) achieved from the simulations and measurements [19]. As seen in this figure, a reasonable match is attained between the computed results and laboratory data. For illustration, an example of an undrained cyclic triaxial stress-controlled test with cyclic stress ratio (*CSR*) = 0.2 is displayed in Fig. 9 to address the response characteristics associated with liquefaction and post-liquefaction axial strain accumulation. It can be seen that the
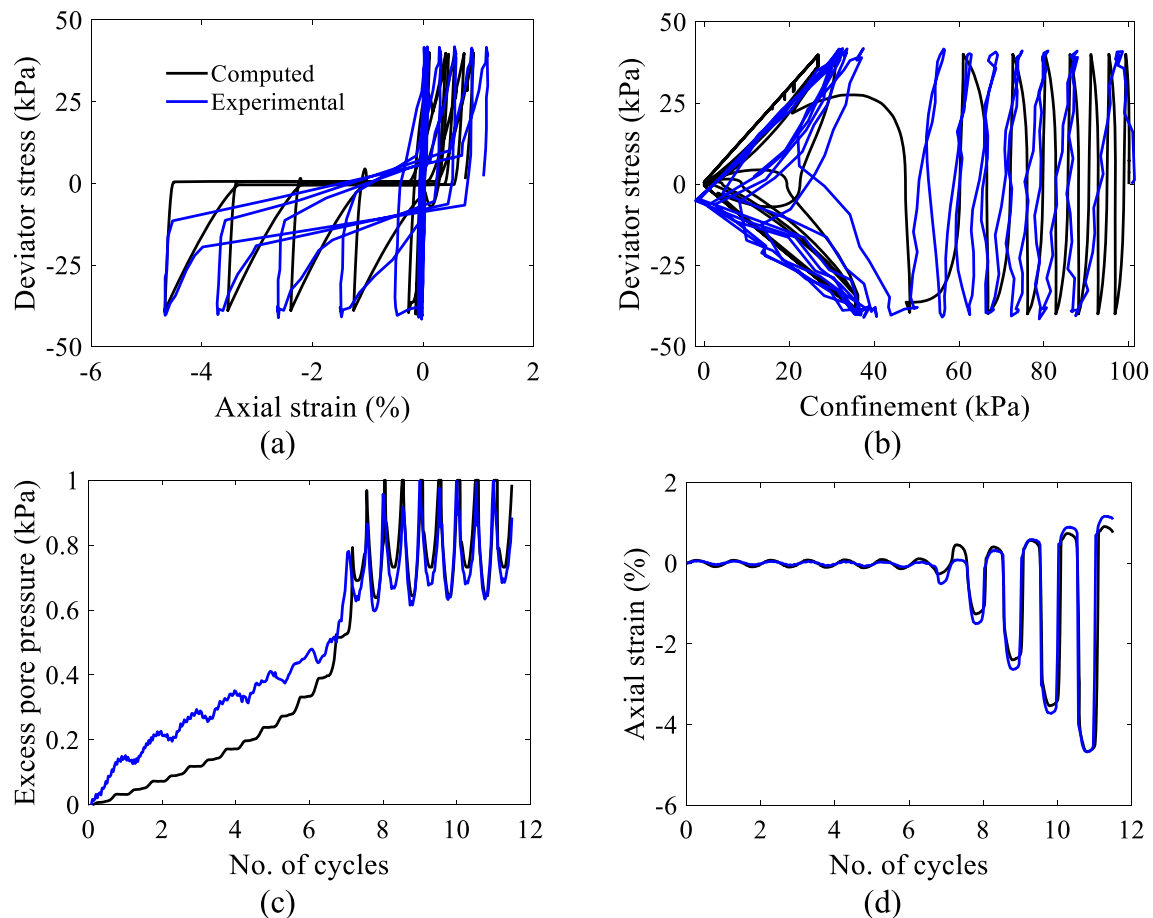
Fig. 9 Laboratory and computed results of undrained stress-controlled cyclic triaxial test with CSR = 0.2 (D_r = 65%): **a** Deviator stress-axial strain; **b** Deviator stress-confinement; **c** Excess pore pressure; **d** Axial strain

computed and experimental results showed a similar asymmetric cycle-by-cycle permanent axial strain accumulation pattern under cyclic stress-controlled triaxial loading conditions (Fig. 9). Nevertheless, the numerical result overestimates the experimental excess pore pressure from small- to medium-strain levels, mainly because the constitutive model parameters associated with dilatancy, and cyclic mobility do not evolve with the soil stress state. This aspect of the model formulation may enhance the volumetric-deviatoric coupling of response. As such, further attention may be given to scrutinize such model response prior to soil liquefaction.

4 Centrifuge test of a liquefiable sloping ground

Using the model parameters in Table 1, numerical simulations are conducted to simulate the dynamic response of a centrifuge test on a liquefiable sloping ground [28, 32]. A

schematic representation of the centrifuge test and the achieved base input motion are shown in Fig. 10. The soil specimen is a sloping layer of Ottawa sand (D_r = 65%) with a 5° inclination. The soil layer built in a container with rigid walls has a length of 20 m and a height of 4 m at its center.

4.1 FE model

A 2D FE mesh (Fig. 10b) comprising 4961 nodes and 4800 quadrilateral elements is created to represent the centrifuge model, and the simulation is performed using the OpenSees. In the FE model, quadrilateral Four-node plane-strain elements (i.e., quadUP) with two-phase material following the $u–p$ [6] formulation are employed for simulating saturated soil response, where u is the displacement of the soil skeleton, and p is the pore water pressure. Earlier studies by Yang and Elgamal [50] highlighted that soil permeability is one of the important factors in affecting the excess pore pressure buildup and accumulation of strains.
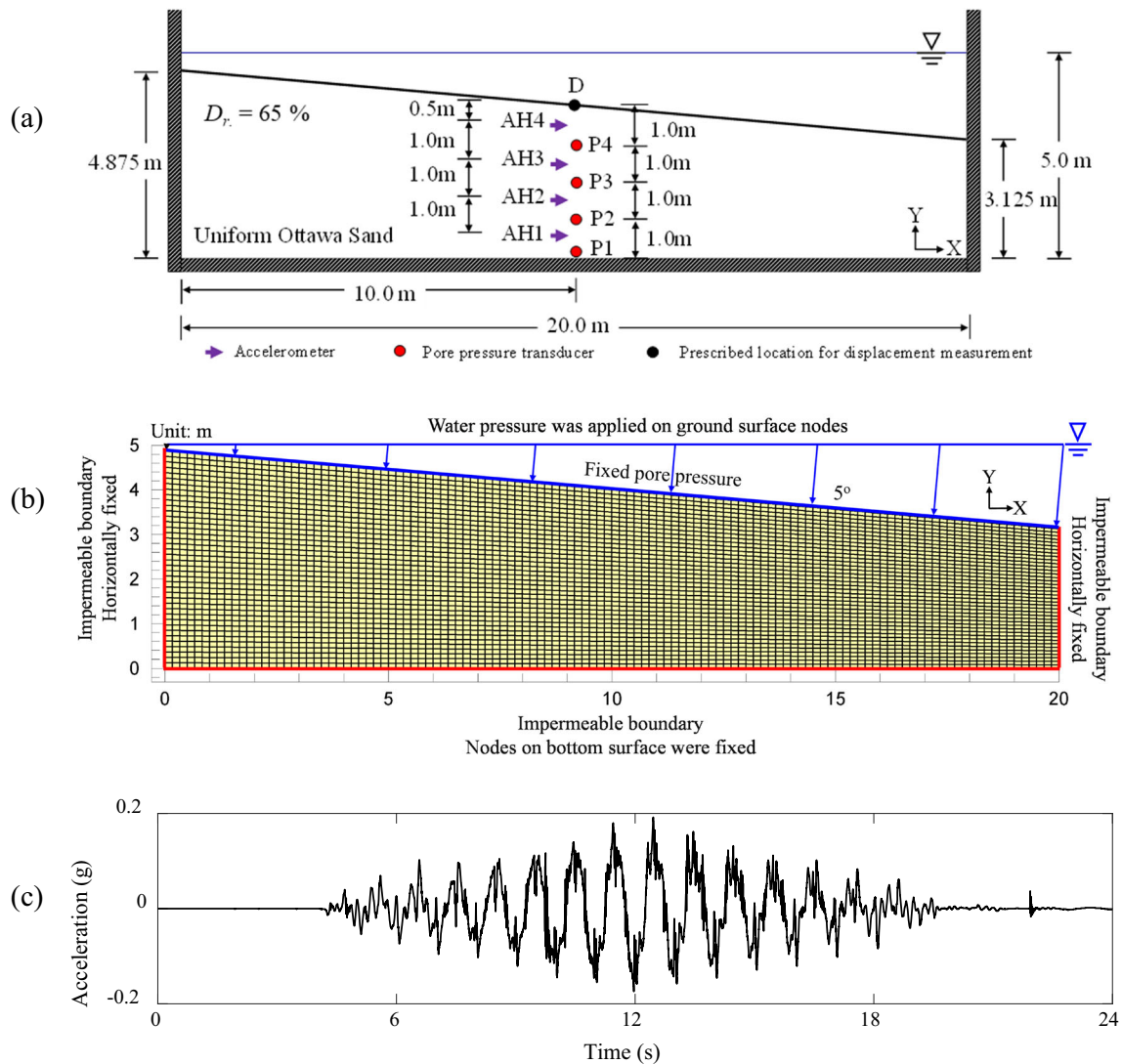
Fig. 10 Centrifuge test of a liquefiable sloping ground: **a** Schematic representation of the experimental layout; **b** FE mesh; **c** Base input motion

In this study, a permeability coefficient of 1.1×10^{-4} m/s is taken for Ottawa sand, as determined by El Ghoraiby et al. [19]. The maximum FE mesh size (about 0.2 m) is selected to resolve waves with frequencies up to 20 Hz, which is considerably larger than the natural frequency (about 1 Hz) of the input motion. Consequently, an element size of about 0.2 m is chosen to be 25 times smaller than the highest frequency of interest (i.e., at least 25 nodes per wavelength).

4.2 Boundary and loading conditions

The boundary and loading conditions [37] for dynamic analysis of the FE model are implemented as follows:

(1) Gravity analysis is performed with linear elastic properties to activate the initial static state: (i) nodes on both side boundaries are fixed against longitudinal translation only, (ii) nodes are fixed horizontally and vertically along the model base, (iii) water table is specified with associated water pressure and nodal forces along the ground surface nodes, and water flow is restricted to across the container boundaries (i.e., impermeable).

(2) Soil properties of the Ottawa sand are shifted from elastic to plastic (Table 1). Subsequently, internal variables of the constitutive model are adjusted to this stress state.
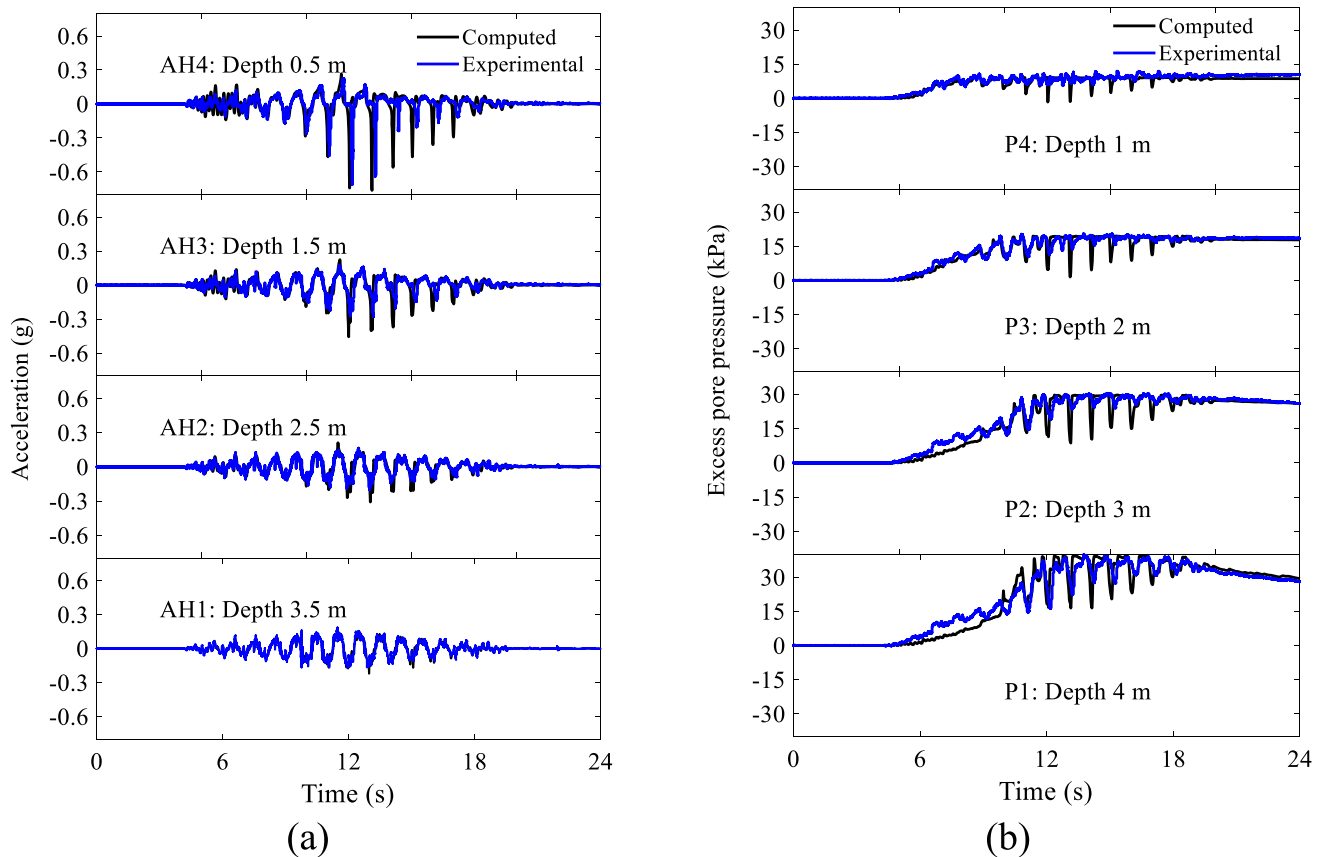
Fig. 11 Experimental and computed time histories: **a** Acceleration; **b** Excess pore pressure

(3) Dynamic analysis is performed by applying the achieved acceleration (Fig. 10c) time history to the FE model base.

In addition, the FE matrix equation of the sloping ground model is integrated by using the Newmark scheme with a time step $\Delta t = 0.01$, and the integration parameters are taken as $\beta = 0.3$ and $\gamma = 0.6$ as suggested by Chan [6]. Although adding numerical damping causes a loss of the second order accuracy of the Newmark scheme, little impact is exerted on the overall computed results [35]. The modified Newton–Raphson method is employed with Krylov subspace acceleration [5] to solve the FE matrix equation. For convergence criteria, a test of energy increment norm of 10^{-4} is used. In addition, a relatively low value of stiffness-proportional viscous damping (coefficient = 0.005) is employed to enhance the numerical stability of FE system, with the majority of damping emanating from the soil nonlinear hysteretic response of the soil (Fig. 7).

4.3 Comparison results

Figure 11a depicts the computed and experimental acceleration time histories at the locations of AH1-AH4 (Fig. 10a). It can be seen that the computed accelerations are in good agreement with those from the measurements. Particularly for shallower depths (AH3 and AH4), both the computed results and measurements showed a consistent trend for acceleration spikes due to dilation.

The excess pore pressure time histories at the locations of P1–P4 (Fig. 10a) are illustrated in Fig. 11b. As seen in this figure, the computed results reasonably match those from the measurements. Overall, the excess pore pressure gradually increased and reached a peak value at about 12 s, indicating loss of effective confinement due to liquefaction (Fig. 11b). In addition, both the computed results and measurements exhibited a consistent trend of negative spikes, in accordance with the acceleration (Fig. 11a).

Figure 12a displays the computed and experimental horizontal displacement time histories at the midpoint of
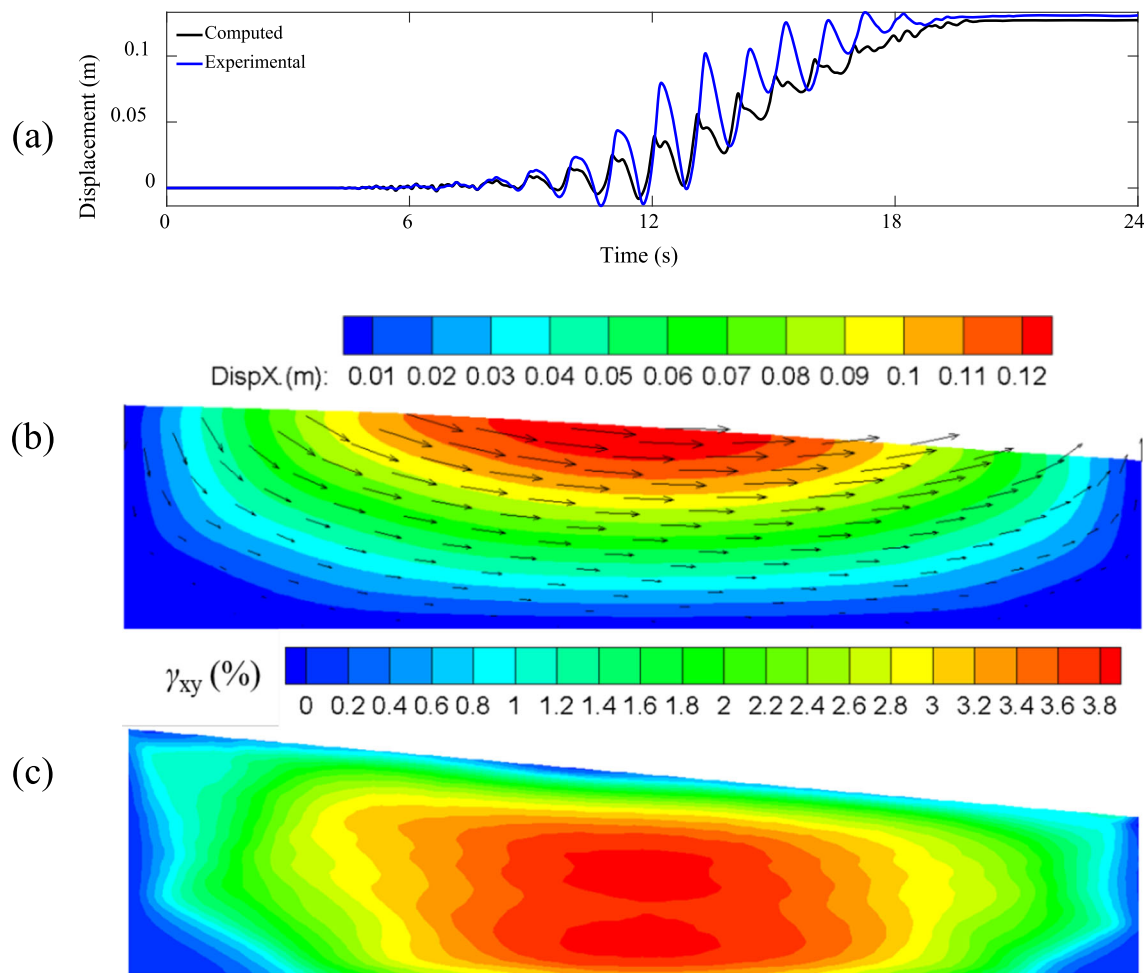
Fig. 12 Slope deformation: **a** Displacement time history at the midpoint of the ground surface; **b**, **c** Computed displacement and shear strain component γ_{xy} contours at the end of shaking

the ground surface (point D in Fig. 10a). It is observed that the computed and experimental results showed a similar cyclic-by-cycle permanent displacement accumulation pattern. At the end of shaking, Fig. 12b depicts the lateral displacement contour with arrows displaying the direction of ground movement, reaching about 0.12 m near the ground surface. In accordance with displacement, Fig. 12c illustrates the shear strain contour with a peak value of about 4% at the middle of the slope.

4.4 Computed soil response

For illustration, Fig. 13 depicts the computed shear stress versus mean effective stress, and shear stress versus shear strain for integration points at the same locations of P1–P4 (Fig. 10a). In Fig. 13a, a cycle-by-cycle downslope shear

strain accumulation pattern can be seen clearly. In addition, the spikes in shear stress appear to be consistent with the excess pore pressure dips due to dilation, as shown in Fig. 11b.

5 Three-dimensional bridge abutment in liquefiable sloping ground

5.1 Ground configuration

In addition to the element and centrifuge level simulations presented earlier, FE simulations are performed to highlight the effects of earthquake-induced liquefaction on a typical bridge abutment in sloping ground using the calibrated parameters shown in Table 1. Figure 14 displays the
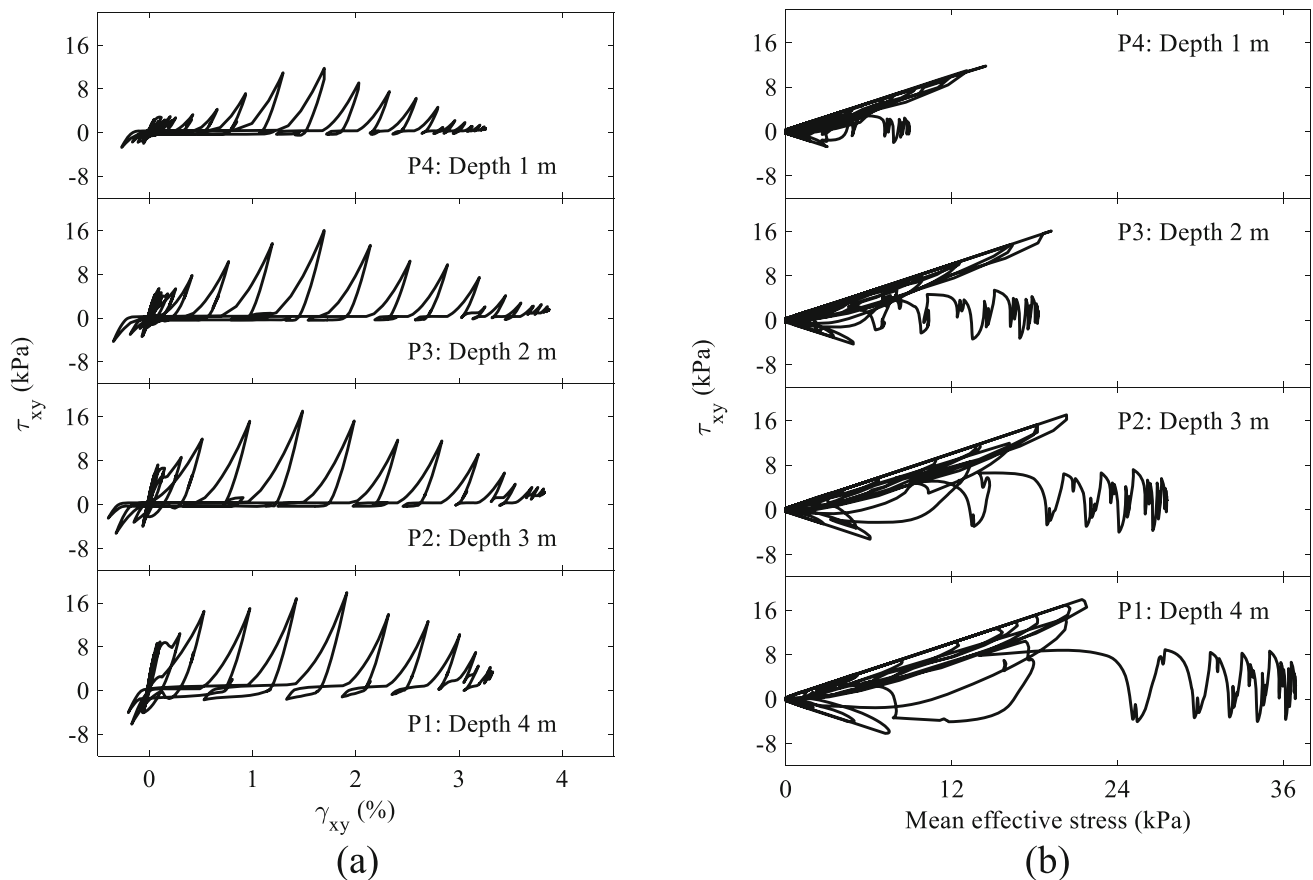
Fig. 13 Computed soil response at locations of P1–P4 (Fig. 10a): **a** Shear stress–strain; **b** Mean effective stress-shear stress

ground configuration of the bridge abutment considered in the FE analysis (similar to the configuration as presented in Shantz [42]), with slope inclination at 2H:1 V (Horizontal: Vertical) in X–Y and Y–Z planes (Fig. 14b). Between X = 40 m and X = 240 m, the ground is configured to have a mildly inclined slope (about 3°) over a distance of 200 m (Fig. 14), to numerically explore more salient response characteristics under earthquake shaking. The soil profiles are idealized into three layers, i.e., an upper fill layer (Table 2), a liquefiable sand layer (D_r = 65%) underlain by a very dense sand layer (D_r = 95% in Table 1 with the same permeability = 1.1×10^{-4} m/s as $D_{r,}$ = 65%). Since the main purpose of this section is to investigate the earthquake-induced liquefaction effects on bridge abutment response, the nonlinear behavior of the upper non-liquefiable fill is idealized and simulated by PIMY material (Table 2) in which the plasticity exhibits only in the deviatoric stress–strain response. In addition, the water table (Fig. 14) is prescribed at the top of the liquefiable sand layer (i.e., elevation = 23 m).

5.2 FE model

Figures 14 and 15a depict the bridge abutment supported on a pile group consisting of 12 cast-in-place-steel-shell (CISS) piles (0.61 m diameter and pile spacing = 2.44 m). The piles are modeled using 3D nonlinear force-based beam-column elements with fiber-section (Fig. 15b). In this fiber section formulation, OpenSees uniaxial material [33] Concrete01 is employed to simulate the core concrete, and Steel02 is used to simulate the reinforcement steel and shell. Figure 15c displays the P-M interaction diagram, where P and M represent axial load and bending moment capacity of the pile foundation. This diagram is particularly useful for investigating the pile strength by the variation of axial loads and bending moments. For illustration, moment–curvature for the pile section under different axial load levels is displayed in Fig. 15c.

For the purpose of this investigation, seismic excitation is applied only in the longitudinal X-direction (i.e., no transverse Z-direction or vertical Y-direction shaking is
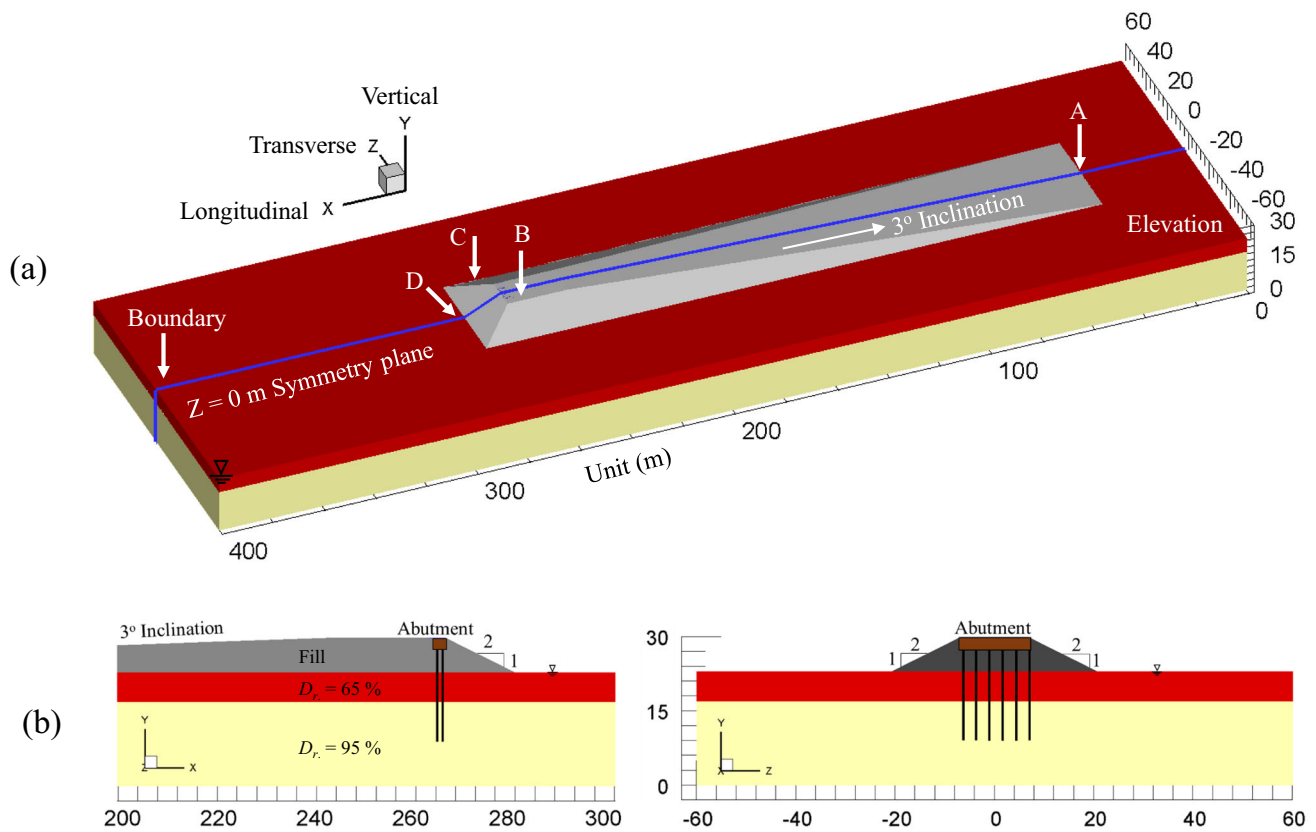
Fig. 14 Abutment configuration: **a** Isometric view; **b** Longitudinal and transverse sections

Table 2 Fill (PIMY in OpenSees) model parameters (Fig. 14)

Model parameters	Fill
Mass density, ρ (t/m^3)	2.1
Cohesion, c (kPa)	60.0
Shear strain at maximum shear strength, γ_{max}	0.1
Low-strain shear modulus, G_o (MPa)	60.0
Poisson's ratio, v	0.4

imparted). As such, a 3D FE half mesh is employed due to symmetry (Figs. 14a and 16). For the boundary condition in the transverse Z-direction, an additional 40 m wide soil domain is included to simulate the 3D slope response away from the bridge abutment. On this basis, the 3D FE mesh (Fig. 16) is generated comprising 97,728 nodes, 92,103 brick elements (i.e., brickUP in OpenSees), and 126 non-linear beam-column elements. For simplicity, rigid beam-column links, normal to the pile longitudinal axis, are used to represent the geometric space occupied by each pile (Fig. 16). The outer nodes of these rigid links are connected to the 3D brick elements using the OpenSees

equalDOF constraint for translational degrees of freedom [33]. Finally, the same FE analysis conditions including nonlinear solver, time-stepping algorithm and damping coefficient are employed as those discussed above.

5.3 Boundary and loading conditions

Along both mesh boundaries (X = 0 m and X = 400 m in Fig. 16), 2D plane strain soil columns of large size (about 100 m in the X-direction) and depth (about 10^7 m in the Z-direction) are included to simulate the free-field motion. These soil columns with identical soil profiles (Fig. 16) are connected to both sides of 3D FE model by using the OpenSees command equalDOF at the same depth, reproducing the desired shear beam free-field response at both side boundaries [38, 39]. In addition, nodes along the symmetry plane (Z = 0 m) and free-field boundary at Z = 60 m are fixed against transverse translation only (i.e., roller conditions at these planes).
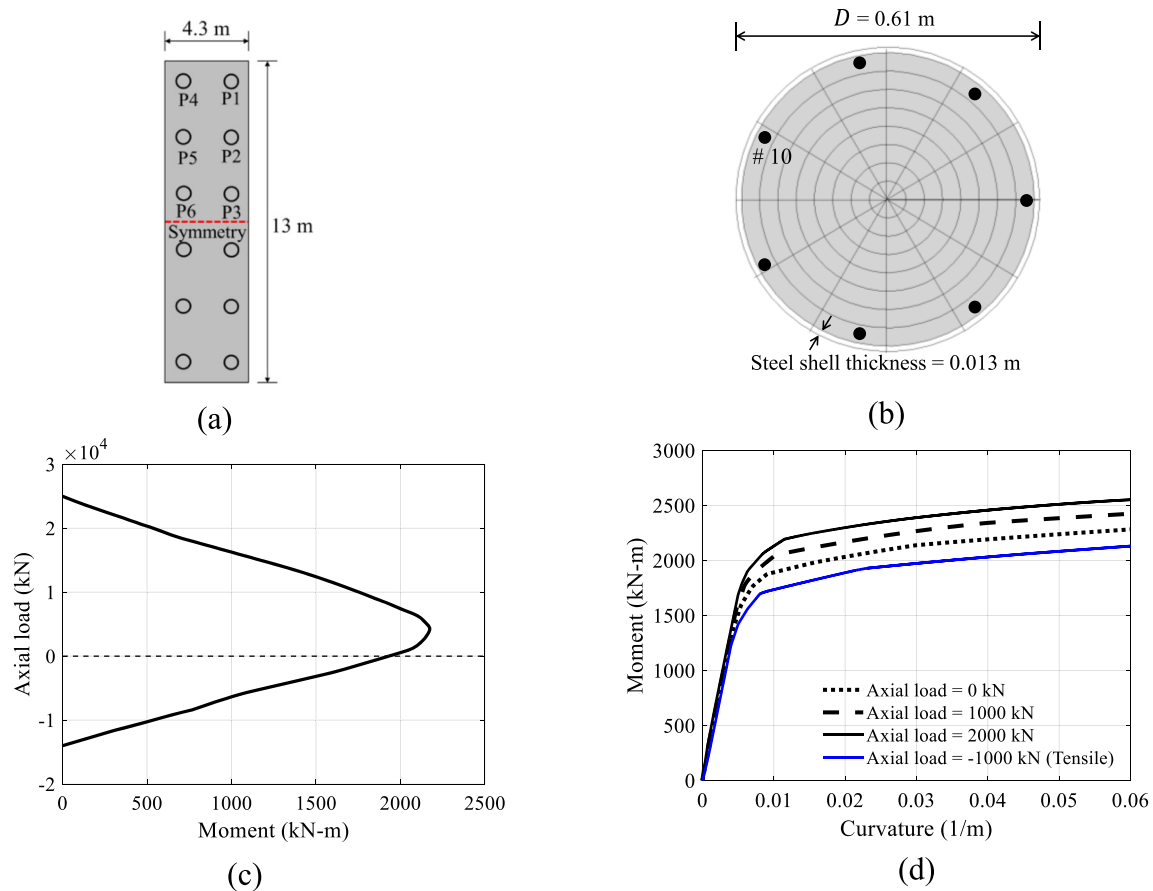
Fig. 15 Pile group: **a** Plan view; **b** Fiber section; **c** Axial load-moment interaction diagram; **d** Moment–curvature at various load levels

In this study, the base of the soil domain (Y = 0 m) is located at a depth of 30 m from the ground surface, about 10 m away from the pile foundations embedded into the very dense sand layer. At the boundary, Lysmer-Kuhlemeyer [31] dashpots defined through the OpenSees ZeroLength element are applied along the base of the FE model in the longitudinal X-direction at each node to avoid spurious wave reflections. For this study, deconvolution (using Shake91 by Idriss and Sun [23]) is employed as a simple approach to derive an incident earthquake motion. As such, the incident seismic wave excitation is defined by dynamic equivalent nodal forces F (Fig. 16b), computed by dashpot coefficient scaled by the area of FE model base. The dashpot coefficient [34] is obtained as the product of the shear wave velocity and mass density of the underlying stratum. Details of this process are presented earlier in Zhang et al. [57] and Elgamal et al. [14].

A realistic input motion is selected for the shaking phase (purely in the longitudinal X-direction) to demonstrate the underlying earthquake-induced liquefaction effect on the 3D bridge abutment deformations. The seismic motion (Fig. 17a) is simply taken as that of the 1989 Loma Prieta earthquake ground surface Lick Observatory Station record (Component 0), with a peak amplitude of 0.44 g. Finally, deconvolution is employed using Shake91 [23] and the achieved incident earthquake motion is imparted [38, 39] along the base of the FE model (elevation 0.0 in Fig. 16).

6 Computed results

6.1 Acceleration response

Figure 17 displays computed acceleration time histories near the ground surface at locations: A, B, D, and boundary, respectively. It can be seen that the acceleration time histories show consistent spikes at about 3.5 s in the liquefiable sand layer (D_r. = 65%) due to dilation. Post that, reduced higher frequency response is noted (starting at about 5 s), mainly due to nonlinear response and soil liquefaction (discussed below).
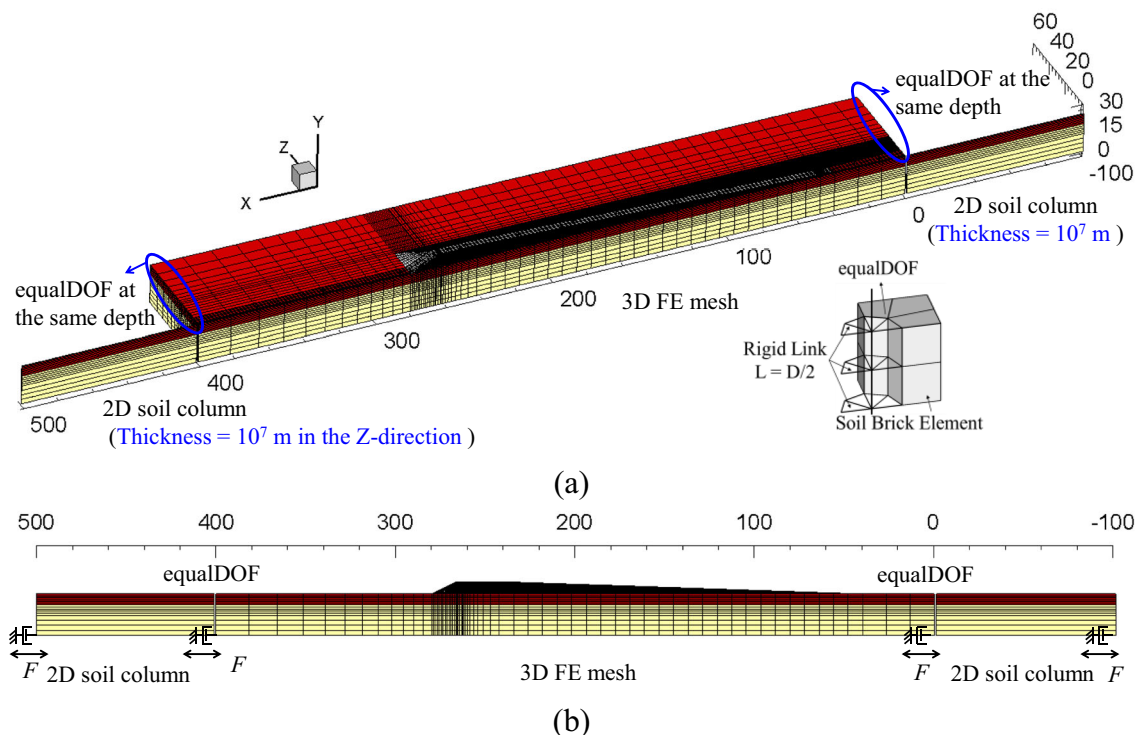
Fig. 16 FE model of the 3D bridge abutment: **a** Isometric view; **b** Side view (symmetry plane)

6.2 Three-dimensional slope deformation

Figure 18 depicts the longitudinal relative displacement contours at the end of shaking (arrows displaying the direction of ground movement), while a clearer picture of the accumulated longitudinal displacement at locations of boundary, A, B and D is depicted in Fig. 19. As seen in these figures, it is noted that:

(1) At both side boundaries (X = 0 m and X = 400 m), longitudinal ground surface deformation is insignificant, only reaching about 0.0006 m (Fig. 19a).

(2) Near the bridge abutment, longitudinal downslope displacement reaches a peak value of about 0.18 m (X = 280 m), due to earthquake-induced liquefaction (as discussed below) and to the dynamic response of the abutment—soil embankment system. The higher local downslope deformation has been frequently observed in reconnaissance investigations [10, 30, 44], and previous numerical studies [20, 27, 36, 38, 39, 55].

(3) Away from the abutment (X = 40 m), permanent downslope displacement is seen reaching about

− 0.1 m, due to the mild 3° slope inclination (Fig. 14a).

(4) The foundations exerted a significant restraining effect on ground deformations, with displacements in the back of foundations (e.g., Location D at X = 260 m) being noticeably lower than those in front of the foundations (e.g., Location B at X = 280 m).

To further illustrate the salient 3D slope deformation pattern, transverse (Z-direction) and vertical (Y-direction) displacement contours at the end of shaking are displayed in Fig. 20. Due to the geometric features of the 3D bridge abutment and the influences of longitudinal local downslope deformation, transverse displacement is clearly observed, reaching a maximum value of about 0.16 m (Figs. 20b and 21b). Furthermore, peak slope settlements near the bridge abutment show slumping by as much as 0.12 m (Figs. 20a and 21a).

6.3 Liquefaction and shear strains

Figure 22 shows time histories of effective confinement p' divided by the initial value p'_0 (before shaking) near the
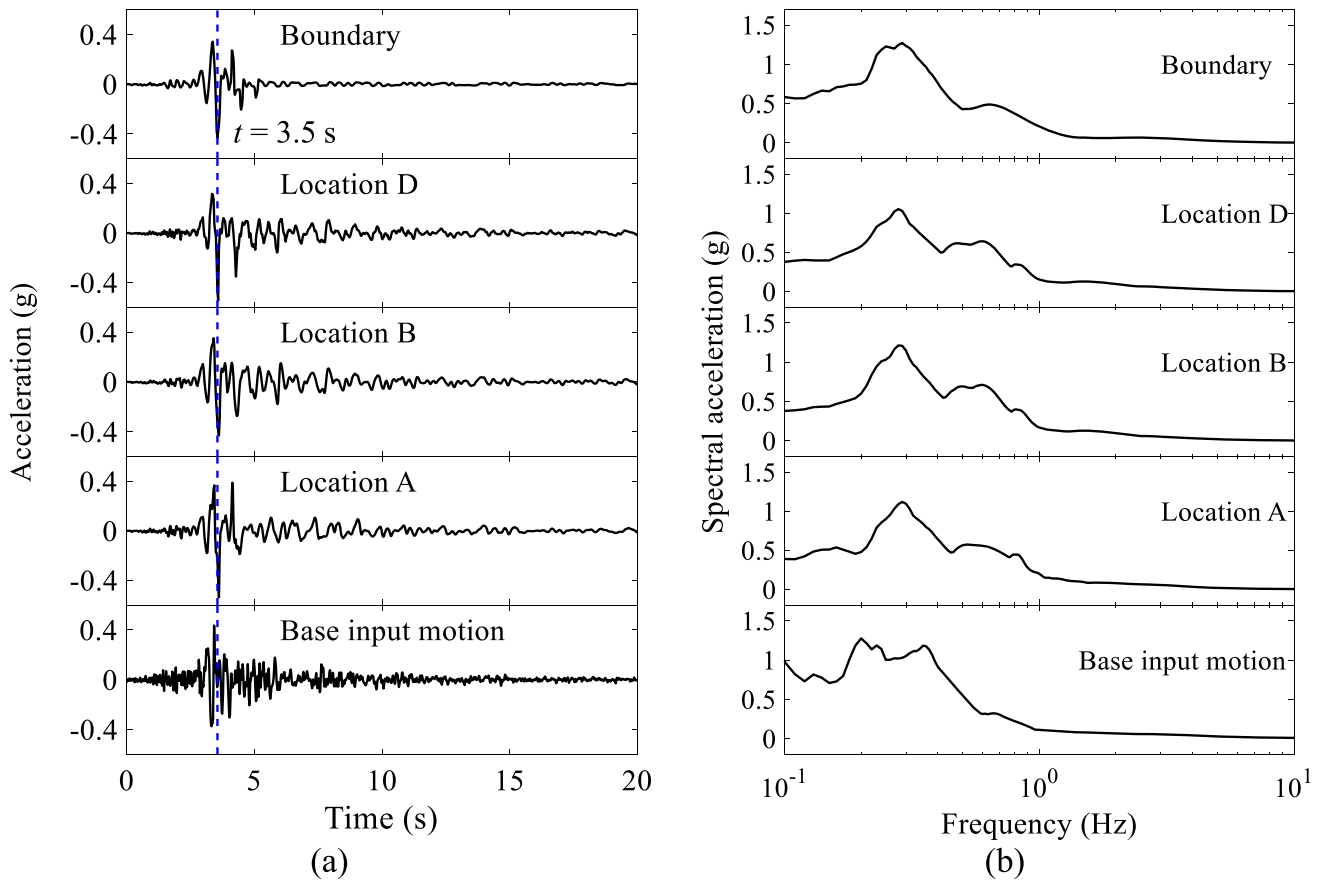
Fig. 17 Acceleration response: **a** Time histories; **b** Spectra (5% damped)
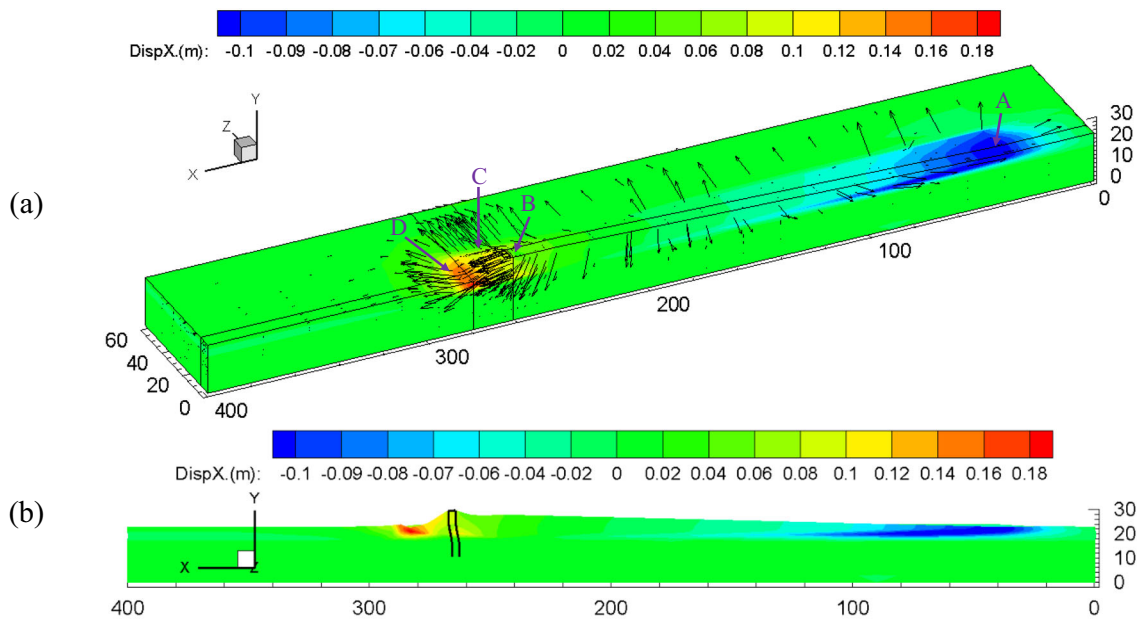

Fig. 18 Longitudinal displacement contours at the end of shaking: **a** Isometric view (arrows displaying direction of ground movement; scale factor of the deformed shape = 20); **b** Side view
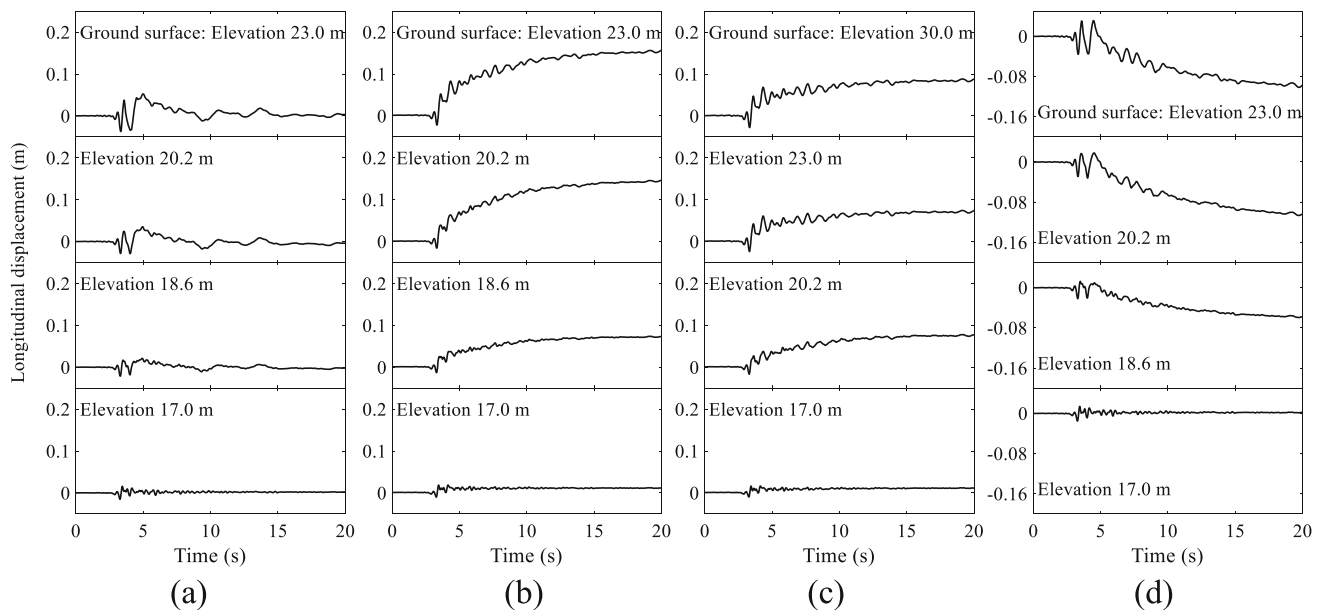
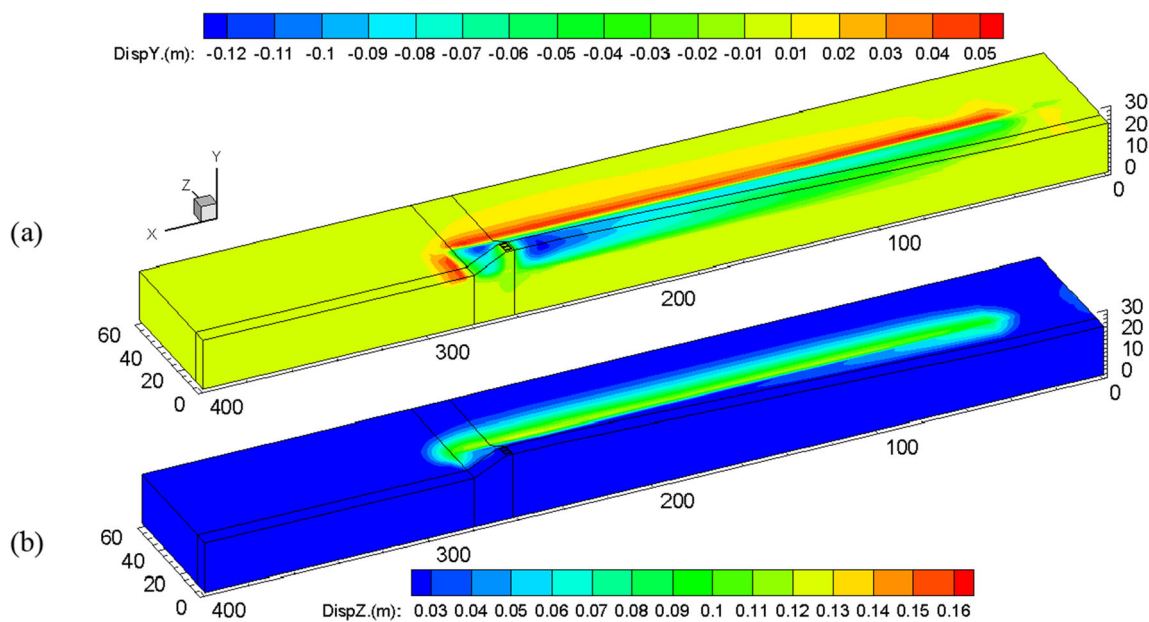Fig. 19 Longitudinal displacement time history: **a** Boundary; **b** Location D; **c** Location B; **d** Location A

Fig. 20 Displacement contours at the end of shaking: **a** Vertical; **b** Transverse

base of the liquefiable sand layer at locations of A, B, D, and boundary (elevation = 19 m), respectively. It can be seen that the ratio p'/p'_0 at boundary reached 0 at about 5 s indicating loss of effective confinement due to liquefaction. Thereafter, the liquefiable sand at the boundary attains its low specified residual shear strength of 0.3 kPa at zero $p'/$

p'_0 (Fig. 22 and Table 1). In accordance with the above deformation, loss of effective confinement and associated post-liquefaction downslope shear strain are clearly observed with a cycle-by-cycle pattern at Locations D, B and A in sloping grounds near the abutment.
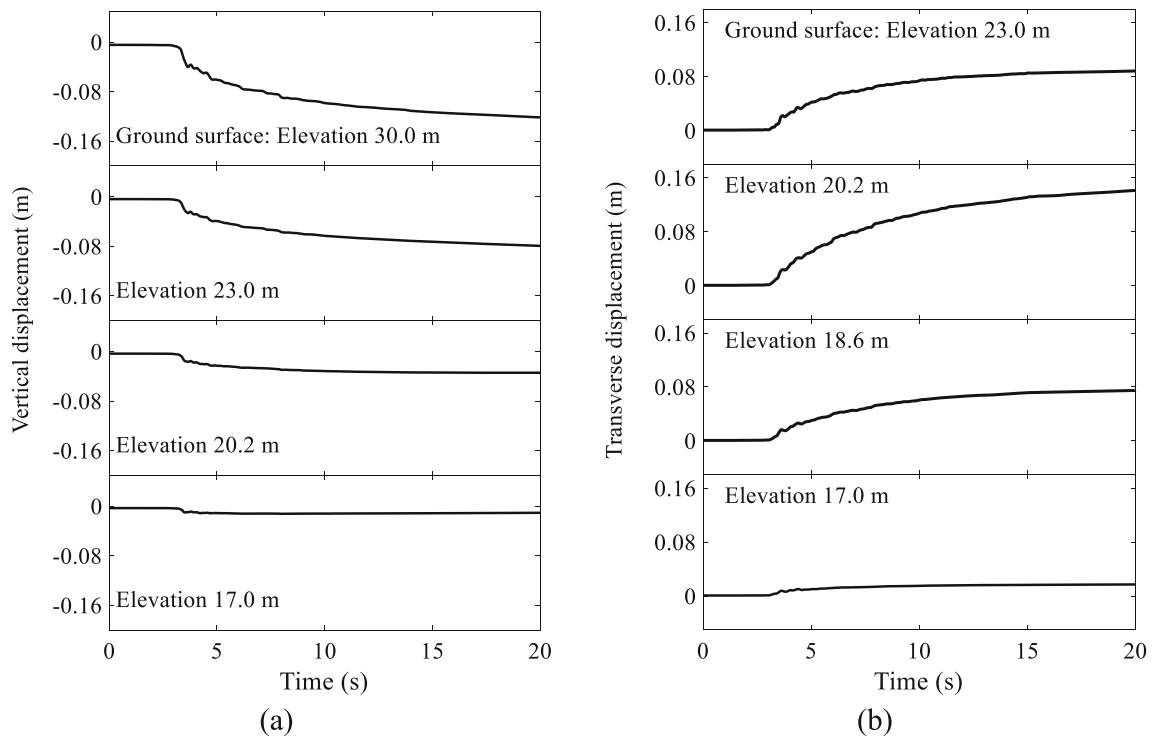
Fig. 21 Vertical and transverse displacement: **a** Location B; **b** Location C
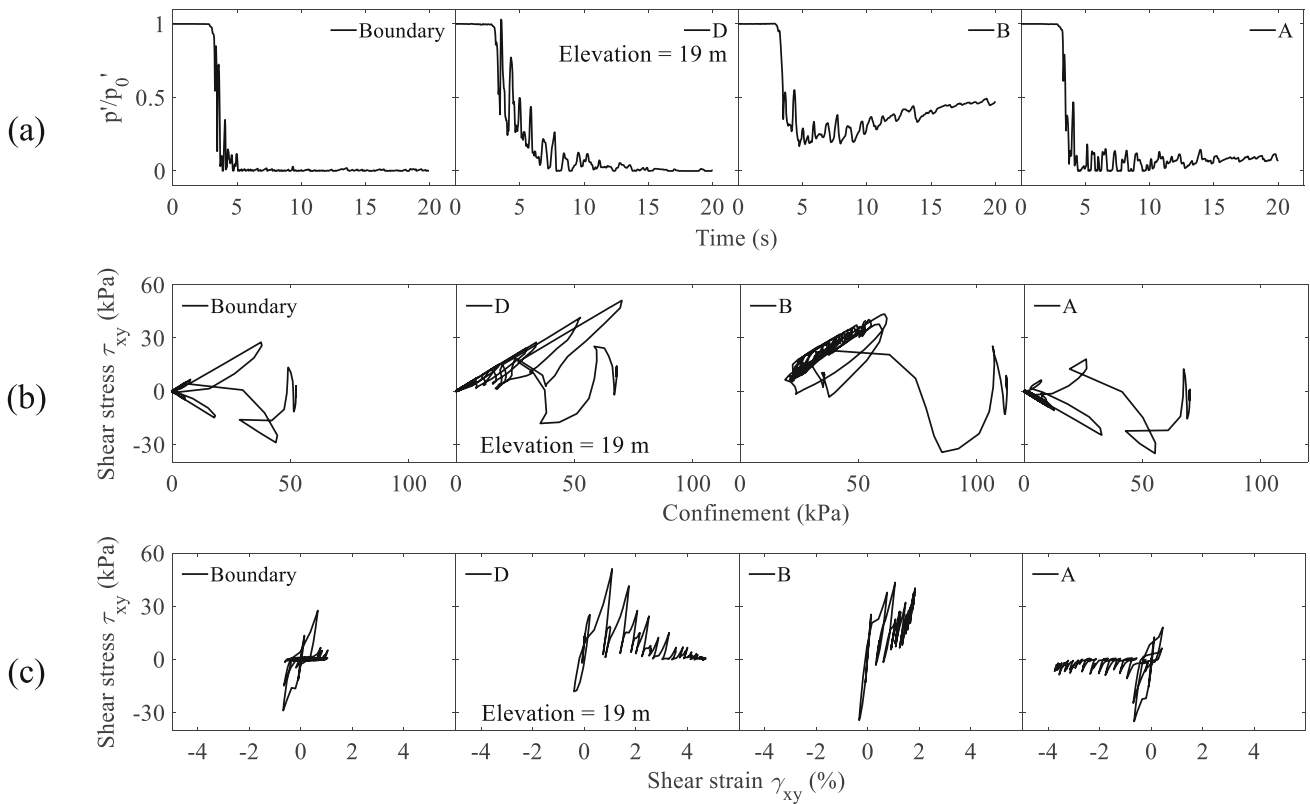

Fig. 22 Soil response near the base of liquefiable layer (elevation = 19 m) at boundary, Locations D, B and A: **a** Ratio of confinement to initial confinement; **b** Shear stress–confinement; **c** Shear stress–strain
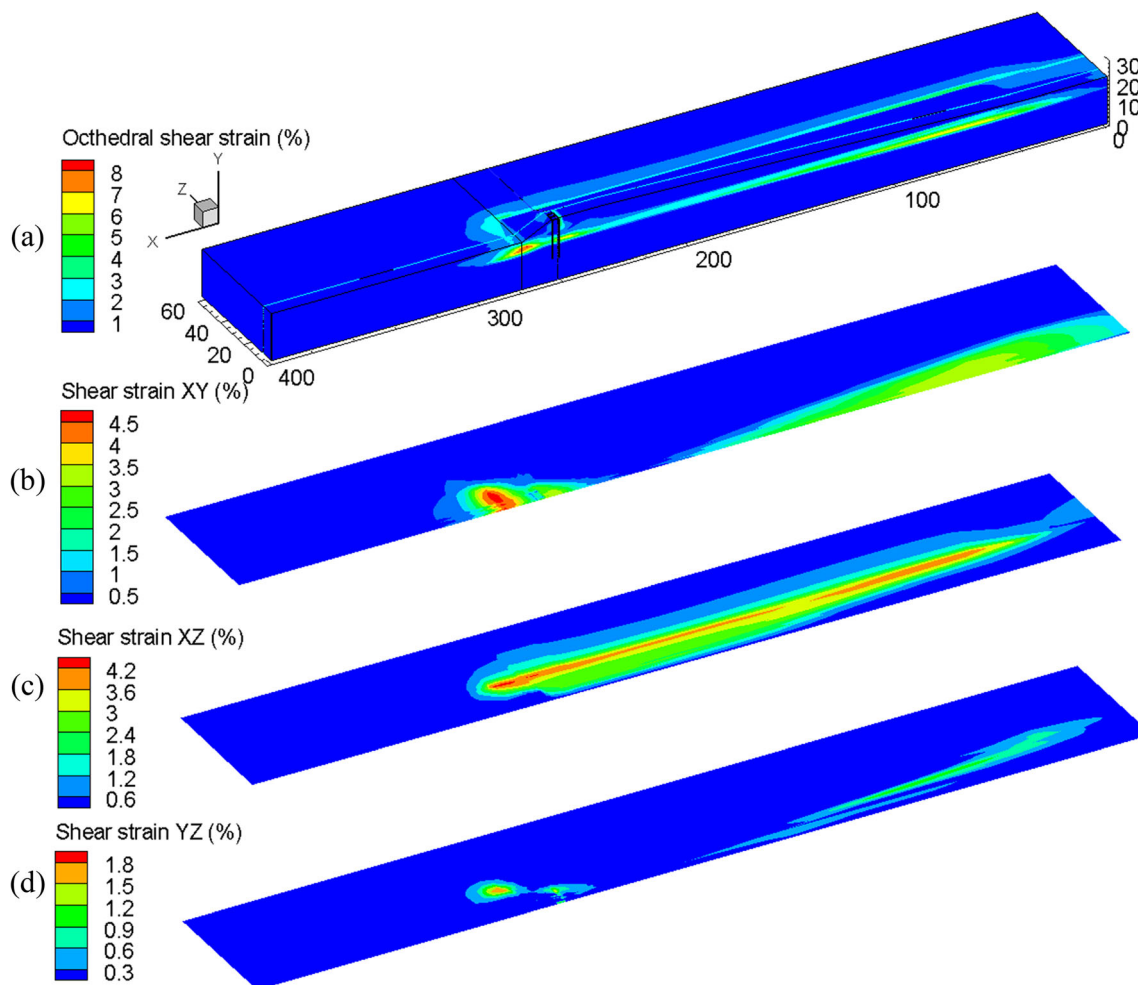
Fig. 23 Shear strain contours at the end of shaking with slices taken at Y = 19 m; **a** Octahedral; **b** Component γ_{xy}; **c** Component γ_{xz}; **d** Component γ_{yz}

In accordance with the above 3D slope deformation pattern, Fig. 23 depicts shear strain contours at the end of shaking, along with three cross-sectional slices at elevation = 19 m. From the overall picture of shear strains (Fig. 23), it may be noted that:

(1) The highest shear strain component γ_{xy} occurred at the steeper slope with inclination 2H: 1 V (Fig. 23b) in front of the bridge abutment (between X = 266 m and X = 280 m). These larger strains correspond to higher downslope ground deformation at these locations (Figs. 18 and 19).

(2) Related to the influence of longitudinal displacement on transverse deformation, Fig. 23c depicts the shear strain component γ_{xz} contour with a XZ cross-sectional slice. As seen in this figure, peak shear strain component γ_{xz} occurred within the slope in the transverse Z-direction (between X = 40 m and X = 300 m), reaching a peak value of about 4.2%.

(3) In accordance with the 3D deformation pattern of this sloping ground (Figs. 18, 19, 20 and 21), high shear strain component γ_{yz} (Fig. 23d) values mainly occurred surrounding the bridge abutment and near the toe of the mildly inclined slope (X = 40 m).

(4) The coupled 3D response mechanisms are further highlighted by the octahedral shear strain as shown in Fig. 23a. Overall, it is observed that shear strain accumulation occurs in all directions.
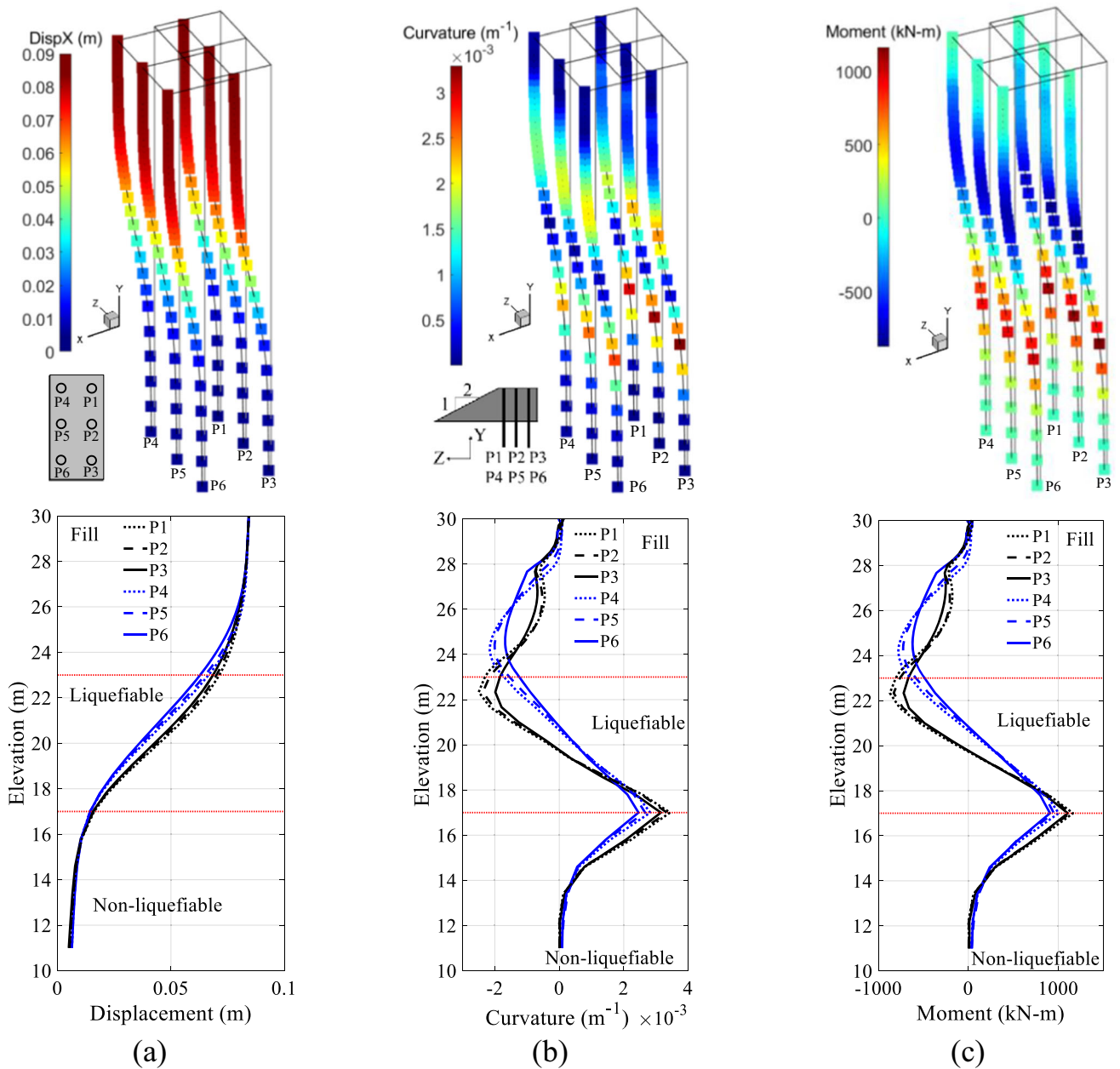
Fig. 24 Pile response at the end of shaking (exaggerated factor = 20): **a** Longitudinal displacement; **b** Curvature; **c** Moment

6.4 Pile response

The pile response is presented in Fig. 24. As discussed above, the dominant ground movement was driven by longitudinal downslope deformation, such that the maximum pile head displacement occurred in the X-direction and reached about 0.09 m (Fig. 24a). Figures 24b and c depicted the curvature and bending moment at the end of

shaking in the XY plane. Generally, it can be seen that the highest curvatures occurred at the interface between liquefied and non-liquefied soils, and the values of the inner piles (P3 and P6) were slightly larger than those of the outer piles (P1, P2 and P4, P5). Additionally, a clearer picture of the curvature and bending moment at these locations (i.e., the interface between liquefied and non-liquefied soils) was displayed in Fig. 25.
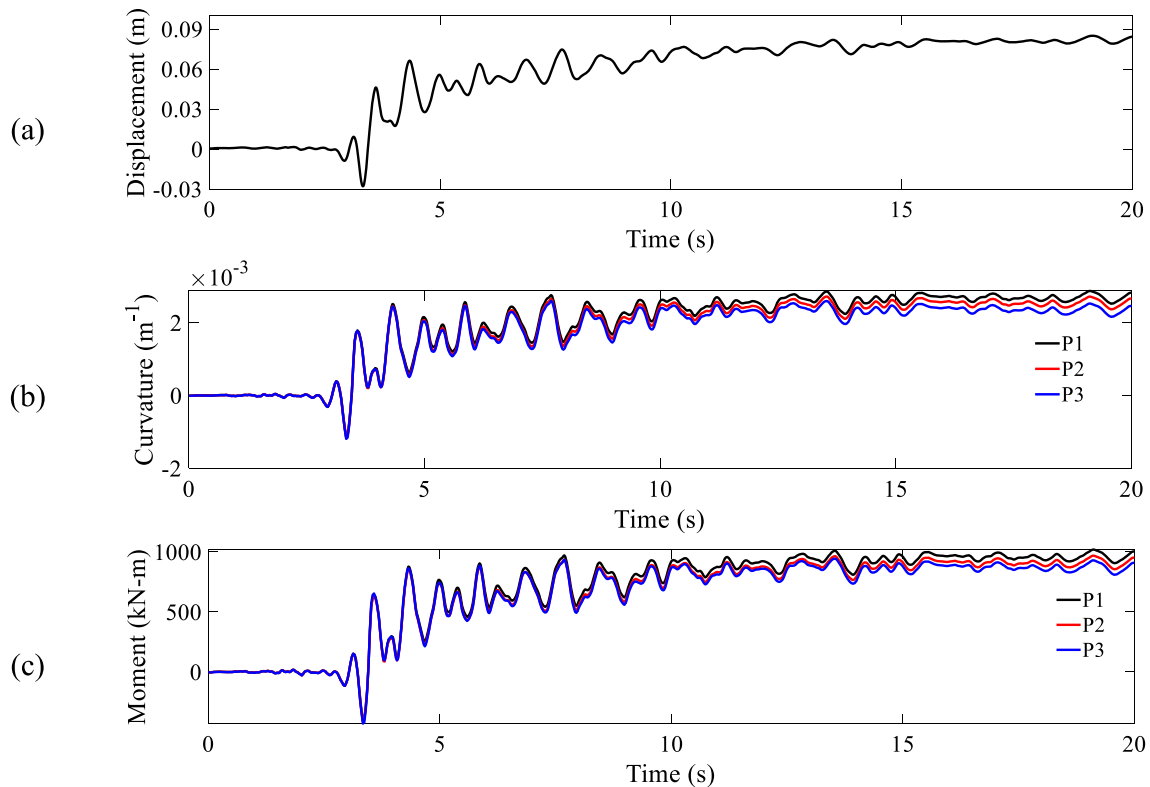
Fig. 25 Time histories: **a** Longitudinal displacement at the top of pile; **b**, **c** Curvature and moment of P1–P3 at the interface between liquefied and non-liquefied soils (elevation = 17 m)

7 Summary and conclusions

This paper presents a 3D multi-surface plasticity model to simulate the liquefaction response of coarse-grained granular soil including cyclic mobility, dilatancy, and post-liquefaction shear strain accumulation. The developed model extends the OpenSees PDMY03 material [26] with the inclusion of Lade–Duncan failure criterion as the essential feature to reproduce salient characteristics of laboratory test data. Subsequently, flow rules are updated for modeling the essential shear response mechanisms, and FE calibrations are undertaken to match a set of laboratory test data, including drained monotonic/undrained stress-controlled cyclic triaxial tests, and a centrifuge test on a liquefiable sloping ground. In addition, full 3D FE simulations of a typical bridge abutment in liquefiable sloping ground are conducted using the calibrated model parameters to highlight effects of soil liquefaction on the ground-structure system. Overall, the developed multi-surface plasticity model provides a useful tool for evaluating earthquake-induced soil liquefaction hazards and associated 3D ground seismic response scenarios.

Specific observations and conclusions are discussed below:

(1) The developed soil constitutive model, including the Lade–Duncan criterion as the yield functions, can reasonably simulate the salient shear response mechanisms of coarse-grained granular soil, discerning the response during triaxial compression and extension.

(2) Implemented with an updated flow rule for contractive, dilative, and neutral phases, the constitutive model realistically captures the liquefaction triggering of Ottawa sand with various relative densities. In addition, the response characteristics of laboratory test data are reasonably reproduced, including undrained stress path and the asymmetric cyclic-by-cycle permanent axial strain accumulation of stress-controlled cyclic triaxial tests.

(3) An overall good match between the FE prediction and centrifuge test results demonstrated that the constitutive model, as well as the employed computational framework OpenSees, have the potential to simulate the seismic response of the liquefiable sloping ground and ultimately realistically evaluate the performance of an equivalent ground system subjected to earthquake-induced liquefaction.

(4) Full 3D FE modeling of liquefiable sloping ground under 3D earthquake excitations might be worth

exploring, given the prevalence of 3D constitutive models. Further parametric studies may be conducted to assess the sensitivity of the numerical results to the geometric configuration of ground and the 3D input motion characteristics.

References

1. Beaty MH, Byrne PM (2011) UBCSAND constitutive model version 904aR. Itasca UDM Web Site, 69
2. Berrill JB, Christensen SA, Keenan RP, Okada W, Pettinga JR (2001) Case study of lateral spreading forces on a piled foundation. Geotechnique 51(6):501–517
3. Borja RI (2006) Condition for liquefaction instability in fluid-saturated granular soils. Acta Geotech 1(4):211–224
4. Boulanger RW, Ziotopoulou K (2013) Formulation of a sand plasticity plane-strain model for earthquake engineering applications. Soil Dyn Earthq Eng 53:254–267
5. Carlson NN, Miller K (1998) Design and application of a gradient-weighted moving finite element code I: in one dimension. SIAM J Sci Comput 19(3):728–765
6. Chan AHC (1988) A unified finite element solution to static and dynamic problems in geomechanics. PhD Thesis, University College of Swansea.
7. Chen L, Ghofrani A, Arduino P (2021) Remarks on numerical simulation of the LEAP-Asia-2019 centrifuge tests. Soil Dyn Earthq Eng 142:106541
8. Chen WF, Mizuno E (1990) Nonlinear analysis in soil mechanics: theory and implementation. Elsevier Science Publisher, Netherlands
9. Cubrinovski M, Ishihara K (1998) State concept and modified elastoplasticity for sand modelling. Soils Found 38(4):213–225
10. Cubrinovski M, Winkley A, Haskell J, Palermo A, Wotherspoon L, Robinson K, Bradley B, Brabhaharan P, Hughes M (2014) Spreading-induced damage to short-span bridges in Christchurch, New Zealand. Earthq Spectra 30(1):57–83
11. Dafalias YF, Manzari MT (2004) Simple plasticity sand model accounting for fabric change effects. J Eng Mech 130(6):622–634
12. Darendeli MB (2001) Development of a new family of normalized modulus reduction and material damping curves. PhD Thesis, University of Texas at Austin
13. Elbadawy MA, Zhou YG, Liu K (2022) A modified pressure dependent multi-yield surface model for simulation of LEAP-Asia-2019 centrifuge experiments. Soil Dyn Earthq Eng 154:107135
14. Elgamal A, Yan L, Yang Z, Conte JP (2008) Three-dimensional seismic response of Humboldt Bay bridge-foundation-ground system. J Struct Eng 134(7):1165–1176
15. Elgamal A, Yang Z, Parra E (2002) Computational modeling of cyclic mobility and post-liquefaction site response. Soil Dyn Earthq Eng 22(4):259–271
16. Elgamal A, Yang Z, Parra E (2003) Modeling of cyclic mobility in saturated cohesionless soils. Int J Plast 19(6):883–905
17. Fuentes W, Wichtmann T, Gil M, Lascarro C (2020) ISA-Hypoplasticity accounting for cyclic mobility effects for liquefaction analysis. Acta Geotech 15:1513–1531
18. Ghofrani A, Arduino P (2018) Prediction of LEAP centrifuge test results using a pressure-dependent bounding surface constitutive model. Soil Dyn Earthq Eng 113:758–770
19. El Ghoraiby M, Park H, Manzari MT (2020) Physical and mechanical properties of Ottawa F65 sand. In: Model tests and numerical simulations of liquefaction and lateral spreading. Springer, Cham, pp 45–67
20. Goel RK (1997) Earthquake characteristics of bridges with integral abutments. J Struct Eng 123(11):1435–1443
21. Hamada M, Isoyama R, Wakamatsu K (1996) Liquefaction-induced ground displacement and its related damage to lifeline facilities. Soils Found 36(Special):81–97
22. Iai S, Tobita T, Ozutsumi O, Ueda K (2011) Dilatancy of granular materials in a strain space multiple mechanism model. Int J Numer Anal Meth Geomech 35(3):360–392
23. Idriss IM, Sun JI (1993) User's manual for SHAKE91: a computer program for conducting equivalent linear seismic response analyses of horizontally layered soil deposits. Center for Geotechnical Modeling, Dept. of Civil and Environmental Engineering, University of California Press, Davis, CA
24. Ishihara K (1985) Stability of natural deposits during earthquakes. In: Theme lecture, proceedings, 11th international conference on soil mechanics and foundation engineering, San Francisco, vol 2, pp 321–376
25. Kabilamany K, Ishihara K (1990) Stress dilatancy and hardening laws for rigid granular model of sand. Soil Dyn Earthq Eng 9(2):66–77
26. Khosravifar A, Elgamal A, Lu J, Li J (2018) A 3D model for earthquake-induced liquefaction triggering and post-liquefaction response. Soil Dyn Earthq Eng 110:43–52
27. Kotsoglou AN, Pantazopoulou SJ (2009) Assessment and modeling of embankment participation in the seismic response of integral abutment bridges. Bull Earthq Eng 7(2):343–361
28. Kutter BL, Zeghal M, Manzari MT (2018). LEAP-UCD-2017 experiments (Liquefaction Experiments and Analysis Projects). DesignSafe-CI [publisher], Dataset. https://doi.org/10.17603/DS2N10S
29. Lade PV, Duncan JM (1975) Elastoplastic stress-strain theory for cohesionless soil. J Geotech Eng Div 101(10):1037–1053
30. Ledezma C, Hutchinson T, Ashford SA, Moss R, Arduino P, Bray JD, Olson S, Hashash YM, Verdugo R, Frost D, Kayen R (2012) Effects of ground failure on bridges, roads, and railroads. Earthq Spectra 28(S1):S119–S143
31. Lysmer J, Kuhlemeyer RL (1969) Finite dynamic model for infinite media. J Eng Mech Div 95:859–878
32. Manzari MT, El Ghoraiby M, Kutter BL, Zeghal M, Abdoun T, Arduino P, Armstrong RJ, Beaty M, Carey T, Chen Y, Ghofrani A (2018) Liquefaction experiment and analysis projects (LEAP): summary of observations from the planning phase. Soil Dyn Earthq Eng 113:714–743
33. McKenna F, Scott M, Fenves G (2010) Nonlinear finite-element analysis software architecture using object composition. J Comput Civ Eng 24(1):95–107
34. Mejia LH, Dawson EM (2006) Earthquake deconvolution for FLAC. In: Paper 04-10. 4th International FLAC symposium on numerical modeling in geomechanics
35. Parra E (1996) Numerical modeling of liquefaction and lateral ground deformation including cyclic mobility and dilation

response in soil systems. PhD Thesis, Rensselaer Polytechnic Institute.

36. Price TE, Eberhard MO (2005) Factors contributing to bridge—embankment interaction. J Struct Eng 131(9):1345–1354

37. Qiu Z, Elgamal A (2020) Numerical simulations of LEAP centrifuge tests for seismic response of liquefiable sloping ground. Soil Dyn Earthq Eng 139:106378

38. Qiu Z, Lu J, Elgamal A, Su L, Wang N, Almutairi A (2019) OpenSees three-dimensional computational modeling of ground-structure systems and liquefaction scenarios. Comput Model Eng Sci 120(3):629–656

39. Qiu Z, Lu J, Ebeido A, Elgamal A, Uang CM, Alameddine F, Martin G (2022) Bridge in narrow waterway: seismic response and liquefaction-induced deformations. J Geotech Geoenviron Eng 148(8):04022064

40. Ramirez J, Barrero AR, Chen L, Dashti S, Ghofrani A, Taiebat M, Arduino P (2018) Site response in a layered liquefiable deposit: evaluation of different numerical tools and methodologies with centrifuge experimental results. J Geotech Geoenviron Eng 144(10):04018073

41. Rapti I, Lopez-Caballero F, Modaressi-Farahmand-Razavi A, Foucault A, Voldoire F (2018) Liquefaction analysis and damage evaluation of embankment-type structures. Acta Geotech 13(5):1041–1059

42. Shantz T (2013) Guidelines on foundation loading and deformation due to liquefaction induced lateral spreading. California Department of Transportation, Sacramento, CA

43. Tsai CC, Hwang YW, Lu CC (2018) Liquefaction, building settlement, and residual strength of two residential areas during the 2016 southern Taiwan earthquake. Acta Geotechica 15:1363–1379

44. Turner BJ, Brandenberg SJ, Stewart JP (2016) Case study of parallel bridges affected by liquefaction and lateral spreading. J Geotech Geoenviron Eng 142(7):05016001

45. Vasko A, El Ghoraiby MA, Manzari MT (2018) Characterization of Ottwa Sand. DesignSafe. https://doi.org/10.17603/DS2TH7Q

46. Verdugo R, Sitar N, Frost JD, Bray JD, Candia G, Eldridge T, Hashash Y, Olson SM, Urzua A (2012) Seismic performance of earth structures during the February 2010 Maule, Chile, earthquake: dams, levees, tailings dams, and retaining walls. Earthq Spectra 28(S1):S75–S96

47. Wang R, Zhang JM, Wang G (2014) A unified plasticity model for large post-liquefaction shear deformation of sand. Comput Geotech 59:54–66

48. Wang R, Cao W, Xue L, Zhang J (2021) An anisotropic plasticity model incorporating fabric evolution for monotonic and cyclic behavior of sand. Acta Geotech 16:43–65

49. Wotherspoon L, Bradshaw A, Green R, Wood C, Palermo A, Cubrinovski M, Bradley B (2011) Performance of bridges during the 2010 Darfield and 2011 Christchurch earthquakes. Seismol Res Lett 82(6):950–964

50. Yang Z, Elgamal A (2002) Influence of permeability on liquefaction-induced shear deformation. J Eng Mech 128(7):720–729

51. Yang Z, Elgamal A (2008) Multi-surface cyclic plasticity sand model with Lode angle effect. Geotech Geol Eng 26(3):335–348

52. Yang Z, Elgamal A, Parra E (2003) Computational model for cyclic mobility and associated shear deformation. J Geotech Geoenviron Eng 129(12):1119–1127

53. Youd TL (1993) Liquefaction-induced damage to bridges. Transp Res Rec 1411:35–41

54. Zeghal M, Goswami N, Kutter BL, Manzari MT, Abdoun T, Arduino P, Armstrong R, Beaty M, Chen YM, Ghofrani A, Haigh S (2018) Stress-strain response of the LEAP-2015 centrifuge tests and numerical predictions. Soil Dyn Earthq Eng 113:804–818

55. Zhang J, Makris N (2002) Kinematic response functions and dynamic stiffnesses of bridge embankments. Earthq Eng Struct Dyn 31(11):1933–1966

56. Zhang JM, Wang G (2012) Large post-liquefaction deformation of sand, part I: physical mechanism, constitutive description and numerical algorithm. Acta Geotech 7(2):69–113

57. Zhang Y, Conte JP, Yang Z, Elgamal A, Bielak J, Acero G (2008) Two-dimensional nonlinear earthquake response analysis of a bridge-foundation-ground system. Earthq Spectra 24(2):343–386

58. Ziotopoulou K (2018) Seismic response of liquefiable sloping ground: Class A and C numerical predictions of centrifuge model responses. Soil Dyn Earthq Eng 113:744–757